

Multi-modal and frequency-weighted tensor nuclear norm for hyperspectral image denoising

Xiaozhen Xie, and Sheng Liu

Abstract—Low-rankness is important in the hyperspectral image (HSI) denoising tasks. The tensor nuclear norm (TNN), defined based on the tensor singular value decomposition, is a state-of-the-art method to describe the low-rankness of HSI. However, TNN ignores some physical meanings of HSI in tackling denoising tasks, leading to suboptimal denoising performance. In this paper, we propose the multi-modal and frequency-weighted tensor nuclear norm (MFWTNN) and the non-convex MFWTNN for HSI denoising tasks. Firstly, we investigate the physical meaning of frequency slices and reconsider their weights to improve the low-rank representation ability of TNN. Secondly, we consider the correlation among two spatial dimensions and the spectral dimension of HSI and combine the above improvements to TNN to propose MFWTNN. Thirdly, we use non-convex functions to approximate the rank function of the frequency tensor and propose the NonMFWTNN to relax the MFWTNN better. Besides, we adaptively choose bigger weights for slices mainly containing noise information and smaller weights for slices containing profile information. Finally, we develop the efficient alternating direction method of multiplier (ADMM) based algorithm to solve the proposed models, and the effectiveness of our models are substantiated in simulated and real HSI datasets.

Index Terms—hyperspectral image, denoising, non-convex approximation, frequency components, multi-modal.

I. INTRODUCTION

HYPERSPECTRAL image (HSI) has been widely used in many fields due to its wealthy spectral information of real scenes, e.g., target detection [1], unmixing [2], classification [3] and so on. Unfortunately, due to imaging conditions and the influence of weather, observed HSIs are often accompanied by the Gaussian noise, salt and pepper noise, and stripe noise. This not only reduces the quality of HSIs, but also hinders subsequent applications. Therefore, to improve the accuracy of subsequent applications, an important research topic is to recover the clear HSI from the observed HSI in the hyperspectral processing tasks [4, 5].

Since the spectral bands are the imaging results of the same scene under different wavelengths, they have global correlation or low-rankness. Based on this prior, HSI can be unfolded into matrices along the spectral mode and then processed by matrix restoration methods. The low-rank matrix recovery-based method restores the clean HSI by minimizing the ranks of unfolding matrices, which is the most popular way [4, 6–8]. Zhang et al. [7] propose to disassemble the noisy HSI into the clean HSI and noise information and use the matrix nuclear norm as the relaxation of the rank function. To improve

the low-rank performance of the model, some non-convex methods are introduced into the HSI denoising task. Xie et al. [9] use the $\log \text{sum}$ function, Chen et al. [10] use the γ function, Lou et al. [11] use the $L_1 - L_2$ function and Gao et al. [12] use the SCAD and MCP function as the non-convex approximation of the rank function. Low-rank matrix decomposition is also an effective way to solve the low-rank minimization problem [13, 14].

However, the unfolding operator destroys the high-dimensional structure of HSI. Treating HSI as a third-order tensor can protect this structure, and tensor rank minimization is the most effective way to overcome the above shortcoming. Due to the non-unique definitions of the tensor rank, different tensor decompositions and the corresponding tensor ranks are proposed, e.g., the CANDECOMP/PARAFAC (CP) decomposition [15, 16], Tucker decomposition [17, 18] and tensor singular value decomposition (t-SVD) [19, 20]. CP rank is defined as the minimum of rank-1 tensors by CP decomposition. Whereas, it is difficult to estimate when HSI is unknown. By Tucker decomposition, a tensor can be decomposed into core tensor and modal matrices. Then, Tucker rank is approximated by the sum of modal matrix nuclear norms (SNN) [18]. However, SNN has shortcomings in preserving low-rank structure, and its results are materially sub-optimal [21, 22].

Due to the powerful representation ability of neural networks, the models based-on deep learning have achieved great achievements in HSI denoising tasks. There are many models that implicitly learn the prior information of HSI from the data, which cannot be represented by traditional regular expressions, e.g., HSI-CNN [23], HSI-SDeCNN [24], HSI-DeNet [25], QRNN3D [26] and so on. The above models explore the prior information of HSI from the perspective of deep network. However, the above models require abundant labeled data for training, which limits their denoising performance by the training data's adversity and quantity [27]. A more suitable strategy is to combine the advantages of deep learning and traditional regularization [27–33].

Based on t-SVD, the tensor tubal rank has attracted extensive attention recently [34–37]. Its convex relaxation is the tensor nuclear norm (TNN), which is defined as the sum of the matrix nuclear norms of each frontal slice in the Fourier transformed tensor [19, 21]. The minimization of TNN can be quickly solved by convex optimization algorithms, and it is effective in characterizing the low-rankness of tensor. Therefore, it is widely used in HSI denoising task [35, 38, 39]. In the definition process of TNN, the information in the image domain of HSI is transformed into frequency information in

Xiaozhen Xie, and Sheng Liu are with College of Science, Northwest A&F University, Yangling 712100, China (e-mail: xiexzh@nwfau.edu.cn (Corresponding author); e-mail: liu_sheng@nwfau.edu.cn).

the Fourier domain. In the Fourier transformed tensor, the low-frequency slices mainly carry the profile information, while the high-frequency slices mainly carry detail and noise information. Besides, in each frontal slice of the Fourier transformed tensor, bigger singular values mainly contain information of clean data and smaller singular values mainly contain information of noise. Meanwhile, HSIs have correlations among different modes, but TNN lacks the flexibility to explore different correlations along with different modes [36]. Thus, it is advantageous to improve the flexibility of TNN when considering the prior information about the physical meaning of frequency, correlation among different modes, and singular value.

In this paper, to take full advantage of the above prior information and improve the capability and flexibility of model, we propose the multi-modal and frequency-weighted tensor nuclear norm (MFWTNN) and non-convex MFWTNN. In the proposed MFWTNN, we explore the physical meaning of frequency to explore the low-rankness of HSI in the Fourier domain and give an adaptive calculation method of frequency weights. In addition, we consider the correlation among the spatial modes and the spectral mode. Furthermore, based on MFWTNN, we take into account the physical meaning of singular values inside frequency slices and propose the non-convex approximation of their nuclear norms. Finally, we apply them to the HSI denoising task. The main contributions of this paper are summarized as follows:

- Motivated by Tucker decomposition, we consider the correlation among spectral and spatial modes of HSI and use the mode- p permutation of tensor instead of the mode- p unfolding matrix. And then we use their weighted sum to explore the low-rankness of HSI. Furthermore, we combine the advantages of multi modes with the improvement of TNN in the frequency domain and propose MFWTNN in HSI denoising.
- In each frontal slice of the Fourier transformed tensor, we choose the *log sum* function as a non-convex approximation to the rank function, which can provide a better approximation to rank function compared with nuclear norms in MFWTNN. Different from the one-dimensional weights of the classical non-convex models, NonMFWTNN considers the weight of frequency direction and singular value direction, which is the two-dimensional weight.
- According to information types in different frequency slices in the Fourier transformed tensor, we adaptively choose bigger weights for slices mainly containing noise information and smaller weights for slices containing profile information, which can depress noise more and simultaneously preserve the profile information of clean HSI better.
- We develop the efficient alternating direction method of multiplier based algorithm to solve the proposed models, and obtain the best restorative performance both on the simulated and real HSI dataset in comparison to all competing HSI denoised methods.

II. NOTATIONS AND PREPARATIONS

A. Notations

In this section, we follow the work in [40, 41] and give some basic notations used about matrix and tensor. We use bold upper-case letter \mathbf{X} and calligraphic letter \mathcal{X} to denote matrix and tensor, respectively. For a 3rd-order tensor $\mathcal{X} \in \mathbb{R}^{n_1 \times n_2 \times n_3}$, its (i, j, k) -th component is denoted as $\mathcal{X}(i, j, k)$. For $\mathcal{X}, \mathcal{Y} \in \mathbb{R}^{n_1 \times n_2 \times n_3}$, their inner product is defined as $\langle \mathcal{X}, \mathcal{Y} \rangle = \sum_{i=1}^{n_1} \sum_{j=1}^{n_2} \sum_{k=1}^{n_3} x_{ijk} y_{ijk}$. Then the Frobenius norm of a tensor \mathcal{X} is computed as $\|\mathcal{X}\|_F = \sqrt{\langle \mathcal{X}, \mathcal{X} \rangle}$. The ℓ_1 -norm of tensor \mathcal{X} was calculated as $\|\mathcal{X}\|_1 = \sum_{i=1}^{n_1} \sum_{j=1}^{n_2} \sum_{k=1}^{n_3} |x_{ijk}|$. The k -th frontal slice of \mathcal{X} is represented as $\mathbf{X}^{(k)} = \mathcal{X}(:, :, k)$. For one-dimensional vector v , its fast Fourier transform is denoted as $\bar{v} = \text{fft}(v) \in \mathbb{C}^N$, and inverse transformation is represented as $v = \text{ifft}(\bar{v})$. For three-dimensional tensor \mathcal{X} , its fast Fourier transform is represented as $\bar{\mathcal{X}} = \text{fft}(\mathcal{X}, [], 3)$ and its inverse operation is $\mathcal{X} = \text{ifft}(\bar{\mathcal{X}}, [], 3)$. The mode- p permutation of \mathcal{X} is defined as $\mathcal{X}_p = \text{permute}(\mathcal{X}, p)$, $p = 1, 2, 3$, where the m -th mode-3 slice of \mathcal{X}_p is the m -th mode- p slice of \mathcal{X} , i.e., $\mathcal{X}(i, j, k) = \mathcal{X}_1(j, k, i) = \mathcal{X}_2(k, i, j) = \mathcal{X}_3(i, j, k)$. Also, its inverse operation is $\mathcal{X} = \text{ipermute}(\mathcal{X}_p, p)$.

B. Problem Formulation

A clean HSI can be treated as a third-order tensor $\mathcal{X} \in \mathbb{R}^{n_1 \times n_2 \times n_3}$ and is usually assumed to be low-rank. Corrupted by mixed noise, its observed version can be modeled as

$$\mathcal{Y} = \mathcal{X} + \mathcal{S} + \mathcal{N}, \quad (1)$$

where $\mathcal{Y}, \mathcal{S}, \mathcal{N} \in \mathbb{R}^{n_1 \times n_2 \times n_3}$; \mathcal{S} denotes the sparse noise; \mathcal{N} denotes the Gaussian white noise.

HSI denoising aims to recover the clean HSI \mathcal{X} from the observed HSI \mathcal{Y} in (1). Under the framework of regularization theory, it can briefly be formulated as

$$\arg \min_{\mathcal{X}, \mathcal{S}, \mathcal{N}} \text{Rank}(\mathcal{X}) + \lambda \|\mathcal{S}\|_1 + \tau \|\mathcal{N}\|_F^2, \text{ s.t. } \mathcal{Y} = \mathcal{X} + \mathcal{S} + \mathcal{N}, \quad (2)$$

where $\|\cdot\|_1$ describes the sparse noise; $\|\cdot\|_F$ describes the Gaussian noise; $\text{Rank}(\cdot)$ represents the rank of unknown ideal HSI; λ and τ are non-negative parameters.

C. Tensor Nuclear Norm

Since the tensor rank function is non-convex and discrete, its rank minimization problem is NP-hard [42]. To overcome computational difficulties, a usual approach is to approximate the non-convex rank function to the convex function and then substitute it into the minimization problem. Fazel [43] proves that the matrix nuclear norm is the convex envelope rank function on the unit sphere of the spectral norm. Thereafter, the nuclear norm is used as a convex replacement of the rank function. The rank minimization problem is transformed into nuclear norm minimization, and it is widely used in low-rank matrix recover based HSI denoising tasks [7].

Furthermore, HSI can be regarded as a third-order tensor. Then, based on t-SVD [19], Lu et al. [21] propose the tensor

nuclear norm (TNN) as the relaxation function of the tensor rank function. TNN is defined as

$$\|\mathcal{X}\|_{\text{TNN}} := \frac{1}{n_3} \sum_{k=1}^{n_3} \|\bar{\mathbf{X}}^{(k)}\|_*, \quad (3)$$

where $\bar{\mathbf{X}}^{(k)}$ is the k th frontal slice of $\bar{\mathcal{X}}$. Due to the property of `fft`, we have

$$\begin{cases} \bar{\mathbf{X}}^{(1)} \in \mathbb{R}^{n_1 \times n_2} \\ \text{conj}(\bar{\mathbf{X}}^{(i)}) = \bar{\mathbf{X}}^{(n_3-i+2)}, i = 2, \dots, \lceil \frac{n_3+1}{2} \rceil \end{cases}. \quad (4)$$

Based on (4), frequency component [37] is defined as

$$\{\bar{\mathcal{X}}_{i-1}\} = \begin{cases} \bar{\mathbf{X}}^{(1)} & \text{if } i = 1 \\ \bar{\mathbf{X}}^{(i)} + \bar{\mathbf{X}}^{(n_3-i+2)} & \text{if } i = 2, \dots, \lceil \frac{n_3+1}{2} \rceil \end{cases} \quad (5)$$

Fig. 1 shows the relationship between the frontal slice and the frequency component.

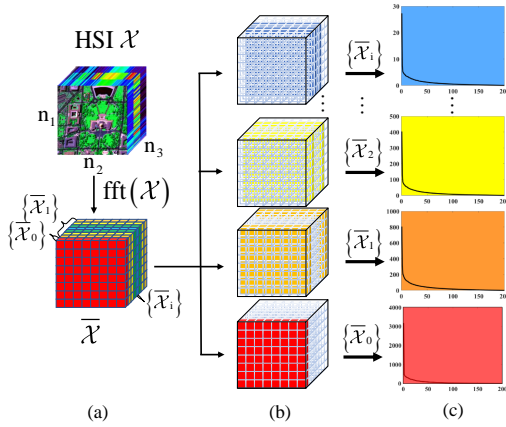


Fig. 1. Illustration of the frequency component. (a) $\bar{\mathcal{X}}$ is the Fourier transform of HSI \mathcal{X} , (b) Frequency component of \mathcal{X} , (c) The singular value curve of the frequency component $\{\bar{\mathcal{X}}_i\}$ of $\bar{\mathcal{X}}$.

Due to TNN can be effective in expressing the low-rank characteristics, it has received extensive attention in the HSI denoising task. However, it focuses on the low-rankness in the spectral dimension. For HSI, its low-rank structure exists with multiple dimensions [41, 44]. To connect the correlation along different dimensions, Liu et al. [18] use modal matrices of the tensor in different directions to explore low-rank structures, and then use SNN as the convex relaxation of the rank function. SNN is defined as

$$\|\mathcal{X}\|_{\text{SNN}} := \sum_{p=1}^3 \alpha_p \|\mathbf{X}_p\|_*, \quad (6)$$

where \mathbf{X}_p is the modal matrix that unfold \mathcal{X} along the direction of the mode- p , α_p is weighting parameter of modes and $\sum_{p=1}^3 \alpha_p = 1$. However, this way will inevitably destroy the internal structure of HSI. Zheng et al. [41] propose the three-directional tensor nuclear norm (3DTNN). They consider the low-rankness of the three modes, which are two spatial modes and one spectral mode. 3DTNN is defined as

$$\|\mathcal{X}\|_{\text{3DTNN}} := \sum_{p=1}^3 \alpha_p \|\mathcal{X}_p\|_{\text{TNN}}, \quad (7)$$

where \mathcal{X}_p is the mode- p permutation of \mathcal{X} . From Fig.2, the

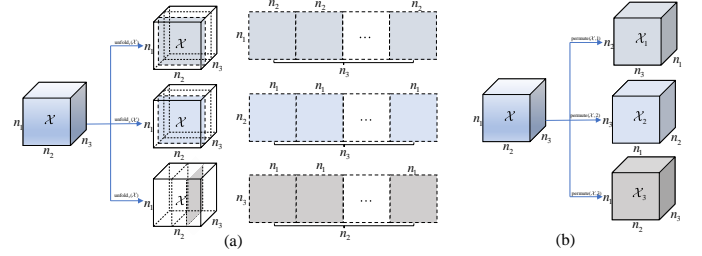


Fig. 2. Mode- p unfolding and mode- p permutation of an $n_1 \times n_2 \times n_3$ tensor.

mode- p permutation is more excellent to explore low-rank structures than the mode- p unfolding for third-order tensor, which avoids the unfolding operator.

III. MULTI-MODAL AND FREQUENCY-WEIGHTED TENSOR NUCLEAR NORM AND ITS NON-CONVEX APPROXIMATION.

A. Multi-modal and Frequency-weighted Tensor Nuclear Norm

In the definition of TNN (3), `fft` plays a core important role in the process of transforming t-products into matrix multiplication in the Fourier domain. It makes TNN to have fast calculation capabilities. However, the role of `fft` is not just for fast computation in the framework of t-SVD. When Fourier matrix \mathbf{F}_n is treated as a transform matrix, $\bar{\mathcal{X}}$ is the feature tensor of \mathcal{X} . There are some similar work which supports this viewpoint [45–52]. To improve the low-rank representation ability of TNN, Wang et al. [37] propose the frequency-filtered tensor nuclear norm (FTNN), which is defined as

$$\|\mathcal{X}\|_{\text{FTNN}} = \frac{1}{I} \sum_{k=1}^I \alpha_k \|\{\bar{\mathcal{X}}\}_k\|_*, \quad I = \left\lceil \frac{n_3+1}{2} \right\rceil \quad (8)$$

where $\|\{\bar{\mathcal{X}}\}_k\|_* = \|\bar{\mathcal{X}}^{(k)}\|_* + \|\bar{\mathcal{X}}^{(n_3-k+2)}\|_*$ is the sum of two matrix nuclear norms, I denotes the number of frequency bands, and α_k is a pre-defined parameter assigned to the k -th frequency band, whose value depends on the prior knowledge. This work treats the FTNN as a frequency filtering method. α_k characterizes the filtering coefficient for the k -th frequency component. However, these parameters should be data-dependent, and the pre-weight parameters cannot well reflect the real physical meaning between filter coefficient and frequency component. For the HSI, it is difficult to give $\lceil \frac{n_3+1}{2} \rceil$ pre-weight parameters in advance. Therefore, we reconsider these weight parameters based on the physical properties of HSI. For the clean Washington DC Mall dataset, sparse noise is added to form clean data, and then the zero-frequency component and non-zero frequency component of the noise data are separated. Fig. 3 shows the grayscale image of the 60th band. We can find an interesting phenomenon that just using the information of the zero frequency component can get satisfactory results without any processing and the noise is more concentrated in the non-zero frequency component. As the transform operator, `fft` plays the role of information separation, which makes the image information and noise

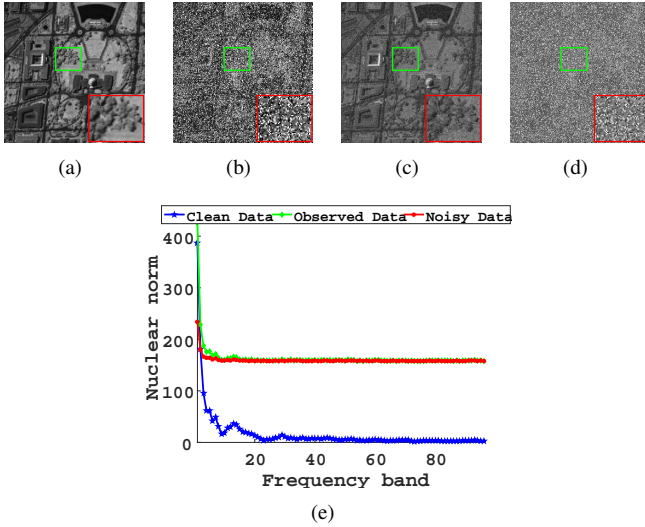


Fig. 3. Recovery of frequency band 60 of Washington DC Mall dataset. (a) clear data \mathcal{X} . (b) observed data \mathcal{Y} . (c) zero frequency component of \mathcal{Y} . (d) non-zero frequency component of \mathcal{Y} . (e) the distribution of clean data, observed data, and noisy data in the frequency domain.

information as separate as possible. The distribution of the nuclear norm shown in Fig. 3(e) is consistent with the observed phenomenon. When the HSI is polluted by noise, the variation in the high-frequency component is bigger than that in the low-frequency component. There is a natural idea that we can reduce the shrinkage of the low-frequency component and increase the penalty of the high-frequency component. Therefore, based on FTNN, we redefine the frequency-weighted tensor nuclear norm (FWTNN):

$$\|\mathcal{X}\|_{FW*} := \sum_{k=1}^{n_3} w_k (\bar{\mathbf{X}}^{(k)}) \|\bar{\mathbf{X}}^{(k)}\|_*. \quad (9)$$

Our weights are different from the weights of FTNN, which are not pre-weight but data dependent. They are discussed in Section III-C.

In the definition of FWTNN, by calculating the nuclear norm along the spectral direction, fft can capture low rank of the HSI spectrum. However, the low-rankness of HSI exists not only in the spectral dimension, but also in the spatial dimensions [18, 44]. Therefore, fft is insufficient in exploring intra-mode and inter-mode correlations of HSI. Besides, in the HSI denoising task, the HSI band may be polluted by stripe noise in the same direction. In a low-rank model that only considers the spectral dimension, these stripe noises will be regarded as part of the low-rank image and are hard to remove. In the frequency domain, for the same HSI, the information expressed by the permuted versions \mathcal{X}_p in different directions is even more different. Therefore, motivated by SNN [18], it is necessary to consider the low-rankness of different modes for HSI denoising task. Different from SNN, to better retain the high-dimensional structures of HSI, its mode- p permutation \mathcal{X}_p to replace its mode- p unfolding matrix \mathbf{X}_p .

Based on the above analysis, we propose the multi-modal and frequency-weighted tensor nuclear norm (MFWTNN) as

follows:

$$\|\mathcal{X}\|_{MFW*} := \sum_{p=1}^3 \alpha_p \|\mathcal{X}_p\|_{FW*} = \sum_{p=1}^3 \sum_{k=1}^{n_3} \alpha_p w_k^p \|\bar{\mathbf{X}}_p^{(k)}\|_*, \quad (10)$$

where $\bar{\mathbf{X}}_p = \text{fft}(\mathcal{X}_p, [], 3)$; $\bar{\mathbf{X}}_p^{(k)}$ is the k -th frontal slice of $\bar{\mathbf{X}}_p$ and its assigned weight is w_k^p ; $\alpha_p > 0$ and $\sum_{p=1}^3 \alpha_p = 1$.

B. Non-convex Multi-modal and Frequency-weighted Tensor Nuclear Norm

In the same frequency slice, its singular values are treated equally. However, the major information of HSI, such as smooth zones and profile, is contained in the larger singular value; the noise information of HSI is contained in the smaller singular value [9–11, 53]. To combine both the frequency and the singular value prior information, we use the log norm to perform non-convex relaxation of the nuclear norm in the frequency band to more accurately describe the tensor rank function [9]. Thus, we propose the non-convex multi-modal and frequency-weighted tensor nuclear norm (NonMFWTNN) to more accurately describe the low-rankness of HSI. It is defined as follows:

$$\begin{aligned} \|\mathcal{X}\|_{MFW*,Log} &:= \sum_{p=1}^3 \alpha_p \|\mathcal{X}_p\|_{FW*,Log} \\ &= \sum_{p=1}^3 \sum_{k=1}^{n_3} \alpha_p w_k^p \log \left(\|\bar{\mathbf{X}}_p^{(k)}\|_* \right), \end{aligned} \quad (11)$$

where $\log \left(\|\bar{\mathbf{X}}_p^{(k)}\|_* \right) = \sum_{i=1}^{n_{12}} \left(\log \left(\sigma_i \left(\bar{\mathbf{X}}_p^{(k)} \right) + \varepsilon \right) \right)$, $n_{12} = \min(n_1, n_2)$. Fig. 4 shows the mechanism of NonMFWTNN. As can be seen from Fig. 4, NonMFWTNN takes into account the relationship between the singular values inside and outside of frequency band. The weights of classic matrix / tensor non-convex models [9, 10, 41, 54] are one-dimensional, which only consider the relationship between the singular values inside the matrix. The way is equivalent to pulling the core singular value matrix $\bar{\mathbf{S}}_p$ in Fig. 4(c) into a column vector and using the weights as the coefficient of this column vector. The weight of MFWTNN is to make a Cartesian product of the weight vector W_F in the frequency direction and the weight vector W_S in the singular value direction, which are two-dimensional weights. If $W_F = 1$, it degenerates to classical one-dimensional weights. The table I shows the distinction and relation between the proposed model and similar work in the weighted parameter. It can be seen from Fig. 4 and table I that the key of the NonMFWTNN is that the core matrix is processed. Liu et.al [55] claim that the core matrix is also low-rank.

C. Frequency-weighted parameter

In the definition of MFWTNN and NonMFWTNN, the values of the frequency-weighted parameter w_k^p are important. The ideal w_k^p can take smaller values that reduce the penalty for the low-frequency slice nuclear norm to protect the main information of HSI in the low-frequency band, and take larger values that increase the penalty for the high-frequency slice

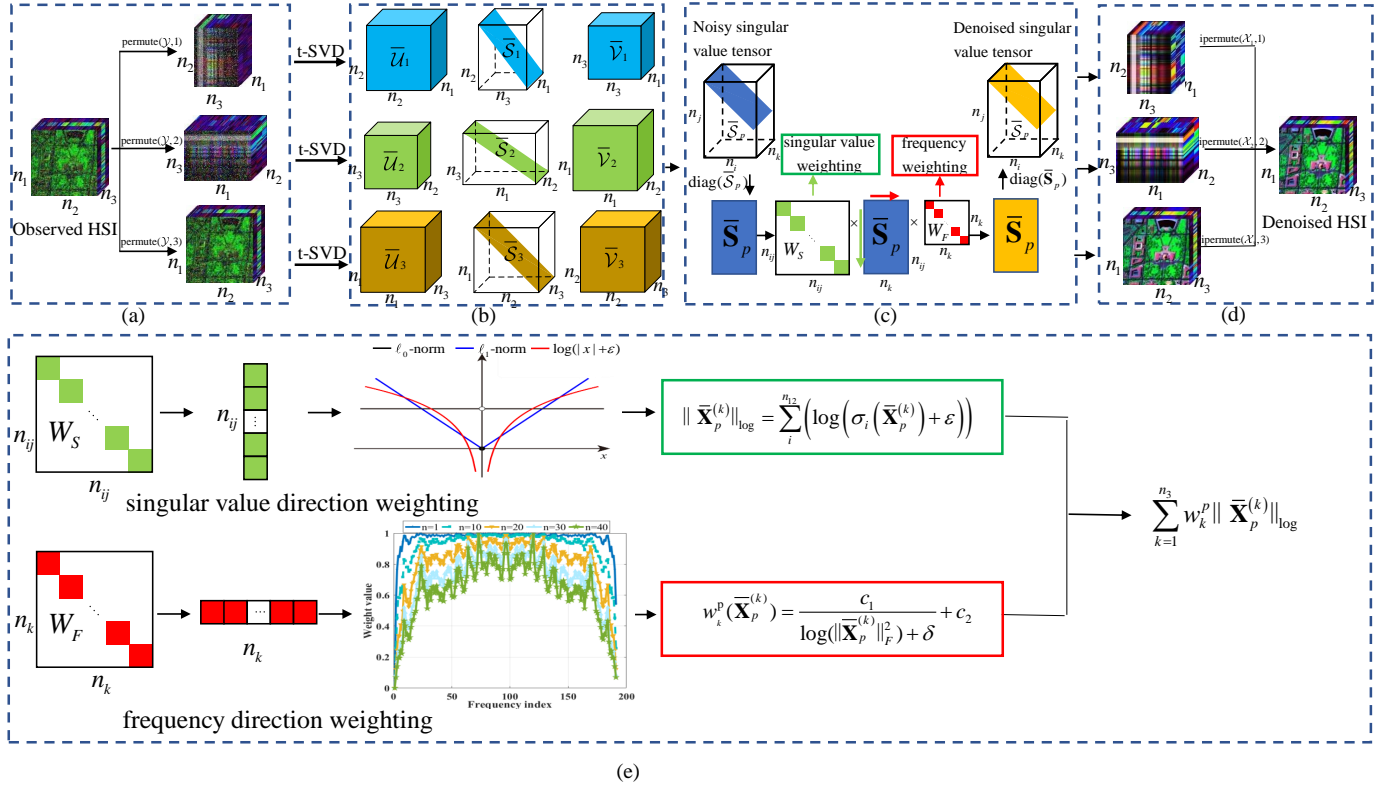


Fig. 4. Illustration of NonMFWTNN. (a) Multi-modal permutations and Fourier transforms. (b) t-SVD of \mathcal{X}_p , $p=1,2,3$. (c) Shrinking the singular value tensor $\bar{\mathbf{S}}_p$, where the size of \mathcal{X}_p is $n_i \times n_j \times n_k$, $n_{ij} = \min(n_i, n_j)$. The horizontal direction is the frequency weighting direction, and the vertical direction is the singular value weighting direction. (d) Synthesis from multi-modal denoised results. (e) The top is the singular value weighting, which is the weight of $\bar{\mathbf{S}}_p$ in the vertical direction. And the bottom is the frequency weighting, which is the weight of $\bar{\mathbf{S}}_p$ in the horizontal direction.

TABLE I
THE DISTINCTION AND RELATION BETWEEN THE PROPOSED MODEL AND SIMILAR WORK IN THE WEIGHTED PARAMETER.

	Modal direction	Singular value direction	Frequency direction
NonMFWTNN	✓	✓	✓
MFWTNN	✓		✓
3DLogTNN[41]	✓	✓	
3DTNN[41]	✓		
FTNN [37]			✓
PSTNN [54]		✓	
TNN [21]			

nuclear norm to fully remove the noise in the high-frequency band. It can be seen from Fig. 5(a) that the nuclear norm is opposite to the distribution characteristics of w_k^p in the frequency domain. It takes larger values in the low-frequency band and takes smaller values in the high-frequency band. And the value of the nuclear norm decreases as the frequency increases. However, the calculation of the nuclear norm brings high cost, which requires singular value decomposition. In a finite dimensional space, any two norms are equivalent. This shows that when transforming from the nuclear norm to the Frobenius norm, they are equal under the normalization condition. Thus, the reciprocal of the Frobenius norm of each frequency slice matrix can be used as w_k^p .

$$w_k^p(\bar{\mathbf{X}}_p^{(k)}) = \frac{1}{\log(\|\bar{\mathbf{X}}_p^{(k)}\|_F^2) + \delta}, \quad (12)$$

where $\delta = 10^{-6}$. The purpose of using log function is to shrink the scale of the value without changing the trend of the Frobenius norm to prevent the extreme influence of the maximum value.

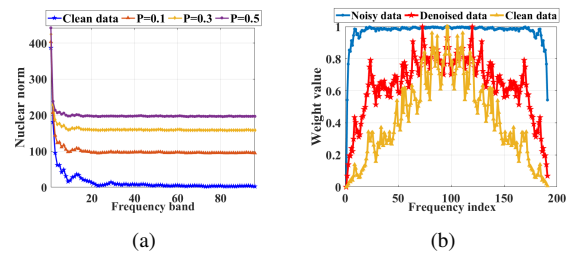


Fig. 5. (a) The distribution of the nuclear norm of each frequency band of DC Mall data under different sparse noise intensities. (b) Frequency weights obtained from different data.

The above method of calculating weights is feasible when the clean HSI is known. However, for HSI denoising tasks, we often only have noisy HSI, and clear HSI is unknown. It can be seen from Fig. 5(b) that the weights calculated by the denoised HSI is closer to the result obtained by the clean HSI than the noisy HSI. Further, as shown in Fig. 4(e), as the number of iterations n continues to increase, the weights calculated by the denoised HSI will get closer to the result of clean HSI. Based on this, we propose an iterative calculation method to update w_k^p . Assuming that the n th iteration gets $\bar{\mathbf{X}}_p^{(k,n)}$, then

the corresponding $w_{k,(n+1)}^p$ of the $n + 1$ th iteration is

$$w_{k,(n+1)}^p = C_1 h_{k,n}^p + C_2, \quad (13)$$

where $h_{k,n}^p = 1/(\log(\|\bar{\mathbf{X}}_p^{(k,n)}\|_F^2) + \delta)$. C_1 is the scaling factor after frequency normalization; C_2 is a constant. Affected by noise, there is less useful information from the denoised HSI in the initial iteration. If it is not corrected, the denoised result will develop in a bad direction. Since TNN is a robust model, inspired by this, we introduce a constant C_2 to improve our weights. When $C_1=0$, it degenerates into TNN. Another reason we introduced C_2 is that noise exists in all frequency bands. The previous conclusion is that there is less noise information in the low-frequency part instead of none. C_2 can achieve a slight shrinkage of all frequency bands. Presetting the value of C_2 is a feasible solution.

IV. HSI DENOISING VIA MFWTNN AND NONMFWTNN MINIMIZATION

A. Proposed model

MFWTNN uses frequency components, modal information, and NonMFWTNN uses the physical meaning of singular value distribution on the basis of MFWTNN. They can provide a better approximation to the tensor rank. Then we use MFWTNN and NonMFWTNN to replace the regularization term Rank in (2) and propose the HSI denoising model as follows:

$$\arg \min_{\mathcal{X}, \mathcal{S}, \mathcal{N}} \sum_{p=1}^3 \alpha_p \|\mathcal{Z}_p\|_{FW*} + \lambda \|\mathcal{S}\|_1 + \tau \|\mathcal{N}\|_F^2, \quad (14)$$

$$s.t. \mathcal{Y} = \mathcal{X} + \mathcal{S} + \mathcal{N}.$$

$$\arg \min_{\mathcal{X}, \mathcal{S}, \mathcal{N}} \sum_{p=1}^3 \alpha_p \|\mathcal{Z}_p\|_{FW*, Log} + \lambda \|\mathcal{S}\|_1 + \tau \|\mathcal{N}\|_F^2, \quad (15)$$

$$s.t. \mathcal{Y} = \mathcal{X} + \mathcal{S} + \mathcal{N}.$$

Introducing auxiliary variables, model (14) and (15) are equivalent to

$$\arg \min_{\mathcal{X}, \mathcal{S}, \mathcal{N}} \sum_{p=1}^3 \alpha_p \|\mathcal{Z}_p\|_{FW*} + \lambda \|\mathcal{S}\|_1 + \tau \|\mathcal{N}\|_F^2, \quad (16)$$

$$s.t. \mathcal{Y} = \mathcal{X} + \mathcal{S} + \mathcal{N}, \quad \mathcal{Z}_p = \mathcal{X}_p, \quad p = 1, 2, 3.$$

$$\arg \min_{\mathcal{X}, \mathcal{S}, \mathcal{N}} \sum_{p=1}^3 \alpha_p \|\mathcal{Z}_p\|_{FW*, Log} + \lambda \|\mathcal{S}\|_1 + \tau \|\mathcal{N}\|_F^2, \quad (17)$$

$$s.t. \mathcal{Y} = \mathcal{X} + \mathcal{S} + \mathcal{N}, \quad \mathcal{Z}_p = \mathcal{X}_p, \quad p = 1, 2, 3.$$

By augmented Lagrangian multiplier method, the Lagrangian function of model (16) can be written as

$$L_{\mu_p, \beta}(\mathcal{X}, \mathcal{Z}_p, \mathcal{N}, \mathcal{S}, \Gamma_p, \Lambda) = \lambda \|\mathcal{S}\|_1 + \tau \|\mathcal{N}\|_F^2$$

$$+ \langle \mathcal{Y} - (\mathcal{X} + \mathcal{S} + \mathcal{N}), \Lambda \rangle + \frac{\beta}{2} \|\mathcal{Y} - (\mathcal{X} + \mathcal{S} + \mathcal{N})\|_F^2$$

$$+ \sum_{p=1}^3 \left\{ \alpha_p \|\mathcal{X}_p\|_{FW*} + \langle \mathcal{X}_p - \mathcal{Z}_p, \Gamma_p \rangle + \frac{\mu_p}{2} \|\mathcal{X}_p - \mathcal{Z}_p\|_F^2 \right\}, \quad (18)$$

where Λ and Γ_p are the Lagrangian multipliers; β and μ_p are the Lagrange penalty parameters. Compared with MFWTNN,

the model based on NonMFWTNN only differs in the steps of solving \mathcal{Z}_p . See the solution of \mathcal{Z}_p for details.

B. Algorithmic optimization

ADMM is an effective framework to solve these type of minimization problems [56]. When other variables are fixed at the n -th iteration, each variable in the Lagrangian function can be updated by solving its corresponding subproblem respectively at the $(n + 1)$ -th iteration.

For \mathcal{Z}_p , $p = 1, 2, 3$, their corresponding subproblems can be written as

$$\arg \min_{\mathcal{Z}_p} \alpha_p \|\mathcal{Z}_p\|_{FW*} + \frac{\mu_p}{2} \left\| \mathcal{Z}_p - \left(\mathcal{X}_p^n + \frac{\Gamma_p^n}{\mu_p} \right) \right\|_F^2. \quad (19)$$

The closed-form solution of (19) obtained from theorem 1 of [37] are as follows:

$$\mathcal{Z}_p^{n+1} = \text{FTSVT}^{w(\mathcal{X}_p^n), \frac{\alpha_p}{\mu_p}} \left(\mathcal{X}_p^n + \frac{\Gamma_p^n}{\mu_p} \right). \quad (20)$$

Similarly, when Rank(\mathcal{X}) is replaced by $\sum_{p=1}^3 \alpha_p \|\mathcal{X}_p\|_{FW*, Log}$ in (17), the sub-problem of \mathcal{Z}_p is rewritten as

$$\arg \min_{\mathcal{Z}_p} \alpha_p \|\mathcal{Z}_p\|_{FW*, Log} + \frac{\mu_p}{2} \left\| \mathcal{Z}_p - \left(\mathcal{X}_p^n + \frac{\Gamma_p^n}{\mu_p} \right) \right\|_F^2. \quad (21)$$

The closed-form solution of (21) obtained from theorem 1 are as follows:

$$\mathcal{Z}_p^{n+1} = \mathcal{DW}^{w(\mathcal{X}_p^n), \varepsilon, \frac{\alpha_p}{\mu_p}} \left(\mathcal{X}_p^n + \frac{\Gamma_p^n}{\mu_p} \right). \quad (22)$$

For \mathcal{X} , its corresponding subproblem can be reformulated as

$$\mathcal{X}^{n+1} = \arg \min_{\mathcal{X}} \sum_{p=1}^3 \frac{\mu_p}{2} \|\mathcal{X} - \mathcal{Z}_p^{n+1} + \frac{\Gamma_p^n}{\mu_p}\|_F^2$$

$$+ \frac{\beta}{2} \|\mathcal{Y} - (\mathcal{X} + \mathcal{S}^n + \mathcal{N}^n) + \frac{\Lambda^n}{\beta}\|_F^2. \quad (23)$$

\mathcal{X} can be updated as follows:

$$\mathcal{X}^{n+1} = \frac{\sum_{p=1}^3 \mu_p \left(\mathcal{Z}_p^{n+1} - \frac{\Gamma_p^n}{\mu_p} \right) + \beta (\mathcal{Y} - \mathcal{S}^n - \mathcal{N}^n + \frac{\Lambda^n}{\beta})}{1 + \beta}. \quad (24)$$

For \mathcal{S} , its corresponding subproblem can be reformulated as

$$\arg \min_{\mathcal{S}} \lambda \|\mathcal{S}\|_1 + \frac{\beta}{2} \|\mathcal{Y} - (\mathcal{X}^{n+1} + \mathcal{S} + \mathcal{N}^n) + \frac{\Lambda^n}{\beta}\|_F^2. \quad (25)$$

It can be solved by the soft-thresholding operator [57] as:

$$\mathcal{S}^{n+1} = \text{shrink} \left(\mathcal{Y} - \mathcal{X}^{n+1} - \mathcal{N}^{n+1} + \frac{\Lambda^n}{\beta}, \frac{\lambda}{\beta} \right). \quad (26)$$

For \mathcal{N} , its corresponding subproblem can be reformulated as

$$\arg \min_{\mathcal{N}} \tau \|\mathcal{N}\|_F^2 + \frac{\beta}{2} \|\mathcal{Y} - (\mathcal{X}^{n+1} + \mathcal{S}^{n+1} + \mathcal{N}) + \frac{\Lambda^n}{\beta}\|_F^2. \quad (27)$$

\mathcal{N} can be updated as follows :

$$\mathcal{N}^{n+1} = \frac{\beta (\mathcal{Y} - \mathcal{X}^{n+1} - \mathcal{S}^n + \frac{\Lambda^n}{\beta})}{2\tau + \beta}. \quad (28)$$

For multipliers Γ_p and Λ , they can be updated as follows:

$$\begin{cases} \Gamma_p^{n+1} = \Gamma_p^n + \mu_p (\mathcal{Z}_p^{n+1} - \mathcal{X}^{n+1}), & p = 1, 2, 3 \\ \Lambda^{n+1} = \Lambda^n + \beta (\mathcal{Y} - \mathcal{X}^{n+1} - \mathcal{S}^{n+1} - \mathcal{N}^{n+1}). \end{cases} \quad (29)$$

C. Time Complexity Analysis

The HSI denoising models based on MFWTNN and NonMFWTNN can be solved by Algorithm 1. Further, we discuss the time complexity of this algorithm. Computing \mathcal{Z}_p , $p = 1, 2, 3$, in both MFWTNN-based solver and NonMFWTNN based solver, has a complexity of $O(n_1 n_2 n_3 \log(n_1 n_2 n_3) + \sum_{i=1}^3 \max(n_i, n_{i+1}) \min^2(n_i, n_{i+1}) n_{i+2})$, where $n_4 = n_1, n_5 = n_2$. Calculating w_k has a complexity of $O(\sum_{i=1}^3 \min(n_i, n_{i+1}) n_{i+2})$. The cost of computing \mathcal{X} , \mathcal{S} , and \mathcal{N} are all $O(n_1 n_2 n_3)$. Then, by calculating the complexity of the above variables, the total complexity of the proposed algorithm can be obtained as $O(n_1 n_2 n_3 \log(n_1 n_2 n_3) + \sum_{i=1}^3 \max(n_i, n_{i+1}) \min^2(n_i, n_{i+1}) n_{i+2} + \sum_{i=1}^3 \min(n_i, n_{i+1}) n_{i+2} + 3n_1 n_2 n_3)$.

Algorithm 1 HSI denoising via the MFWTNN and NonMFWTNN minimization

Input: The observed tensor \mathcal{Y} ; weight parameters c_1, c_2, ε ; regularization parameters λ, τ ; and stopping criterion ϵ .

Output: Denoised image \mathcal{X} .

- 1: Initialize: $\mathcal{Y}=\mathcal{X}=\mathcal{S}=\mathcal{N}=\mathcal{Z}_p$; $\Gamma_p = \Lambda = 0$; $\mu_p=\beta=10^{-3}$; $p = 1, 2, 3$; $\mu_{max} = 10^{10}$; $\rho = 1.2$ and $n = 1$.
 - 2: Repeat until convergence:
 3. Update $\mathcal{X}, \mathcal{S}, \mathcal{N}, \mathcal{Z}_p, \Lambda, \beta, \mu_p, w_k, \Gamma_p$ via
 - step 1: Update \mathcal{Z}_p by (20) or (22)
 - step 2: Update \mathcal{X} by (24)
 - step 3: Update \mathcal{S} by (26)
 - step 4: Update \mathcal{N} by (28)
 - step 5: Update Γ_p, Λ by (29)
 - step 6: Update $\mu_p = \rho\mu_p, \beta = \rho\beta, w_k$ by (13)
 - 4: Check the convergence condition.
-

V. EXPERIMENT RESULTS AND DISCUSSION

In this section, we conduct experiments on simulated and real-world HSIs to substantiate the effectiveness of the proposed MFWTNN and NonMFWTNN model for HSI denoising. For evaluating the effectiveness of the models, our models are compared with six state-of-the-art HSI denoised methods, i.e., LRTA [6], BM4D [58], LRMR [7], LRTDTV [44], 3DTNN [41] and 3DLogTNN [41]. Since LRTA and BM4D are only suitable for removing Gaussian noise and our experiments are to remove hybrid noise, for fair comparison, we first use the RPCA [21] to remove sparse noise, and then use these models to obtain denoised results. Before the experiments, all pixels of models in the HSI band are normalized to [0,1]. In all experiments, the parameters in these comparative methods are manually adjusted according to the suggestions in relevant papers. In Section V-C, the parameters of the proposed models are discussed in detail. We use visual comparison and quantitative comparison to comprehensively evaluate the performance of different denoising methods. In quantitative comparisons, we use five quantitative picture quality indices (PQIs), i.e., PSNR [59], SSIM [60], FSIM [61], ERGAS [62] and SAM [63], to assess the denoised results. Better denoised results correspond to higher values in MPSNR, MSSIM and MFSIM, and lower values in MERGAS and MSAM.

A. Simulated HSI Data Experiments

We select two HSI datasets for the simulated experiments to evaluate the performance of our methods (see Fig. 6). One is collected by the reflection optical system imaging spectrometer (ROSIS-03), which is named the Pavia City Center dataset¹. Its size is 1096×1096 , with a total of 102 bands. The reason we chose a sub-block with a size of $200 \times 200 \times 80$ as a simulation dataset is that some bands are seriously polluted by noise and have lost the meaning of reference. The other one is collected by the HSI acquisition sensor (HYDICE), which is named the Washington DC Mall dataset². Its size is 1208×307 , with a total of 191 bands. We choose a sub-block with a size of $256 \times 256 \times 191$ as a simulation dataset.

The observed HSIs are usually degraded by hybrid noises, i.e. Gaussian noise, sparse noise and stripe noise. Thus, to better simulate the degradation mechanism of HSI, we add various intensities of hybrid noises to clean HSI. In the simulation experiments, hybrid noises with eight different intensity levels are added to the simulation dataset band by band. Let G and P denote the variance of Gaussian white noise and percentage of impulse noise, respectively. In noise cases 1-5, the same intensity noise is added to all the bands. Specifically, in noise case 1, $G=0.1$ and $P=0.2$; in noise case 2, $G=0.1$ and $P=0.3$; in noise case 3, $G=0.1$ and $P=0.4$; in noise case 4, $G=0.15$ and $P=0.2$; in noise case 5, $G=0.2$ and $P=0.2$; in noise cases 6-8, the noise intensities are different for different bands; in noise case 6, $G=0.1$ and P is randomly selected from 0.2 to 0.4; in noise case 7, G is randomly selected from 0.1 to 0.3 and $P=0.2$; in noise case 8, G is randomly selected from 0.1 to 0.3 and P is randomly selected from 0.1 to 0.3. In addition, stripe noises are added to the 54th-64th bands of the Pavia City Center and the 70th-100th bands of the Washington DC Mall.

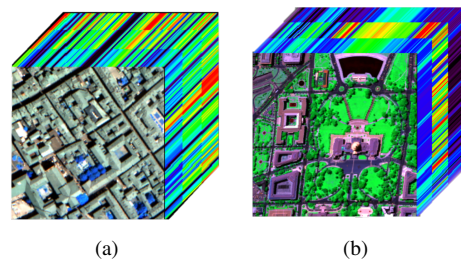


Fig. 6. Datasets used in the simulated experiment. (a) Pavia City Center dataset (R:20, G:50, B:80). (b) Washington DC Mall dataset (R:50, G:80, B:150).

1) Pavia City Center: In this subsection, we show the evaluation results of all denoising models including visual and quantitative quality on the Pavia City Center dataset.

Table II reports quantitative comparison and CPU running time of all the compared methods under the condition of the eight noise cases on the Pavia City Center dataset. When compared to the other methods, our proposed methods obtain the optimal PQIs among all the denoising models in most noise

¹<http://www.ehu.es/ccwintco/index.php/>

²<http://lesun.weebly.com/hyperspectral-data-set.html>

TABLE II
QUANTITATIVE COMPARISON AND TIME OF EIGHT DENOISING MODELS ON PAVIA CITY CENTER DATASET UNDER EIGHT NOISE CASES.

Case	Level	Index	Noise	LRTA	BM4D	LRMR	LRTDTV	3DTNN	3DLogTNN	MFWTNN	NonMFWTNN
Case 1	G=0.1	MPSNR	11.122	29.440	29.701	31.259	32.297	31.696	33.487	32.470	34.398
		MSSIM	0.105	0.905	0.920	0.905	0.914	0.924	0.942	0.928	0.945
		MFSIM	0.510	0.947	0.949	0.946	0.942	0.954	0.964	0.955	0.968
	P=0.2	MERGAS	1013.518	123.549	119.608	99.715	87.316	94.645	77.865	89.194	69.458
		MSAM	45.712	6.805	5.840	6.824	4.930	4.844	4.394	5.656	4.339
		time/s	-	14.013	115.944	116.111	128.850	56.638	86.658	66.917	96.791
Case 2	G=0.1	MPSNR	9.541	28.484	28.864	30.173	31.188	30.657	32.823	31.600	33.420
		MSSIM	0.065	0.887	0.910	0.881	0.897	0.903	0.933	0.915	0.935
		MFSIM	0.452	0.938	0.942	0.935	0.931	0.941	0.958	0.947	0.961
	P=0.3	MERGAS	1216.767	138.09	132.124	112.427	99.239	106.370	83.831	97.753	77.512
		MSAM	47.676	7.204	6.236	7.250	5.349	5.619	4.570	6.065	4.528
		time/s	-	14.006	116.229	109.304	127.285	59.130	89.352	67.251	98.926
Case 3	G=0.1	MPSNR	8.384	27.265	27.745	28.937	29.741	27.696	31.339	30.570	31.879
		MSSIM	0.043	0.859	0.892	0.848	0.873	0.790	0.915	0.898	0.913
		MFSIM	0.411	0.926	0.933	0.920	0.917	0.892	0.945	0.936	0.948
	P=0.4	MERGAS	1390.482	158.869	150.540	128.938	117.629	148.361	99.511	109.129	92.185
		MSAM	48.58	7.629	6.745	7.740	6.007	9.875	5.042	6.506	4.925
		time/s	-	14.197	111.924	113.685	132.354	66.067	94.827	72.480	107.781
Case 4	G=0.15	MPSNR	10.716	27.026	27.420	29.013	30.111	29.089	31.133	30.451	32.021
		MSSIM	0.088	0.848	0.879	0.849	0.867	0.868	0.905	0.891	0.913
		MFSIM	0.483	0.923	0.925	0.921	0.913	0.920	0.942	0.933	0.948
	P=0.2	MERGAS	1060.262	161.397	154.021	127.846	112.153	126.82	101.226	110.568	91.095
		MSAM	46.411	7.825	6.671	7.690	5.848	5.895	5.227	6.562	5.050
		time/s	-	14.683	112.103	112.627	131.750	62.625	94.155	72.962	104.037
Case 5	G=0.2	MPSNR	10.265	25.163	25.619	27.321	28.605	27.009	29.134	29.088	30.520
		MSSIM	0.074	0.789	0.835	0.791	0.821	0.799	0.860	0.856	0.885
		MFSIM	0.461	0.901	0.900	0.898	0.886	0.88	0.917	0.913	0.931
	P=0.2	MERGAS	1115.059	198.966	188.524	154.623	133.338	160.649	126.652	128.254	108.312
		MSAM	46.978	8.379	7.17	8.385	6.685	6.923	5.981	7.143	5.580
		time/s	-	14.355	115.494	117.568	126.082	58.988	88.231	67.559	97.910
Case 6	G=0.1	MPSNR	9.515	28.374	28.761	30.090	31.062	30.400	32.569	31.512	33.405
		MSSIM	0.066	0.885	0.908	0.879	0.895	0.894	0.927	0.913	0.937
		MFSIM	0.452	0.937	0.942	0.933	0.931	0.938	0.956	0.946	0.960
	P=(0.2,0.4)	MERGAS	1235.513	139.857	133.652	113.657	100.96	109.752	86.176	98.851	78.252
		MSAM	47.824	7.278	6.281	7.294	5.501	6.078	4.991	6.148	4.589
		time/s	-	14.490	115.407	116.126	128.118	59.013	87.868	67.084	97.160
Case 7	G=(0.1,0.3)	MPSNR	10.193	25.281	25.589	27.437	28.773	26.772	29.211	29.218	30.800
		MSSIM	0.074	0.803	0.833	0.798	0.826	0.784	0.868	0.861	0.893
		MFSIM	0.461	0.906	0.898	0.900	0.890	0.875	0.920	0.916	0.934
	P=0.2	MERGAS	1131.564	198.204	189.307	153.217	131.728	167.334	126.702	126.994	105.541
		MSAM	47.045	9.057	7.138	8.518	6.650	7.733	6.194	6.885	5.672
		time/s	-	14.881	116.565	116.969	125.336	58.311	87.113	67.129	96.770
Case 8	G=(0.1,0.3)	MPSNR	9.052	24.289	24.653	26.402	27.922	25.048	28.711	28.489	29.332
		MSSIM	0.053	0.770	0.812	0.759	0.803	0.673	0.852	0.839	0.865
		MFSIM	0.425	0.893	0.887	0.884	0.876	0.836	0.913	0.903	0.916
	P=(0.2,0.4)	MERGAS	1299.108	222.242	210.596	172.408	145.080	207.854	134.585	136.996	125.036
		MSAM	48.246	9.538	7.394	9.122	7.027	11.026	7.233	7.689	7.526
		stipes time/s	-	13.861	116.280	113.436	125.442	60.487	88.043	67.376	97.515

cases, indicating the advantage of the proposed methods in HSI denoising. Although LRTA and LRTDTV also consider the low-rankness among different modes, they can not fully exploit the connection among the modes. BM4D use non-local similarity information and LRTDTV use spatial smoothing information. These make the denoised result excessively smooth and lack texture details. Although 3DTNN considers the correlation among different modes, it is still not accurate enough to represent the low-rankness of HSI. 3DLogTNN and MFWTNN use the physical meaning of singular values and frequency components to improve 3DTNN respectively. But these are not the best descriptions of the low-rankness of HSI. NonMFWTNN inherits the advantages of 3DLogTNN and MFWTNN, and improves the ability to express low-rankness of HSI in terms of frequency components and singular values. Although the time complexity of our models is higher, our models have obtained better-denoised results.

In Fig. 7, we show denoised results of the Pavia City Center dataset in terms of PSNR and SSIM for each band under all noisy case experiments. As this figure shows, our methods obtain the optimal PSNR and SSIM values in most bands. In

Fig. 8, we show the 50th band of the denoised results of all comparison methods in case 2. In Fig. 9, we show the 32th band of the denoised results in case 3. As these grayscale images show, LRTA, LRMR and 3DTNN cannot completely remove some high-intensity noises. For BM4D and LRTDTV, although they can remove more noise, they also lose more details. This makes the denoised result too smooth. Compared with them, our proposed models can remove more noise while retaining more details. The spectral signatures are important indicators for HSI. To further compare the denoised image quality, we show the spectral curve of the pixel (170, 99) under case 1 in Fig. 10. It can be seen that spectral signatures curves are relative to ERGAS values in table II, and our models can obtain the optimal value.

2) Washington DC Mall: In this subsection, we show the evaluation results of all denoising models including visual and quantitative quality on the Washington DC Mall dataset under the condition of the eight noise cases.

Table III lists the PQIs of denoised results under eight noise cases in the Washington DC Mall dataset. As this table shows, our proposed models obtain preeminently higher MPSNR and

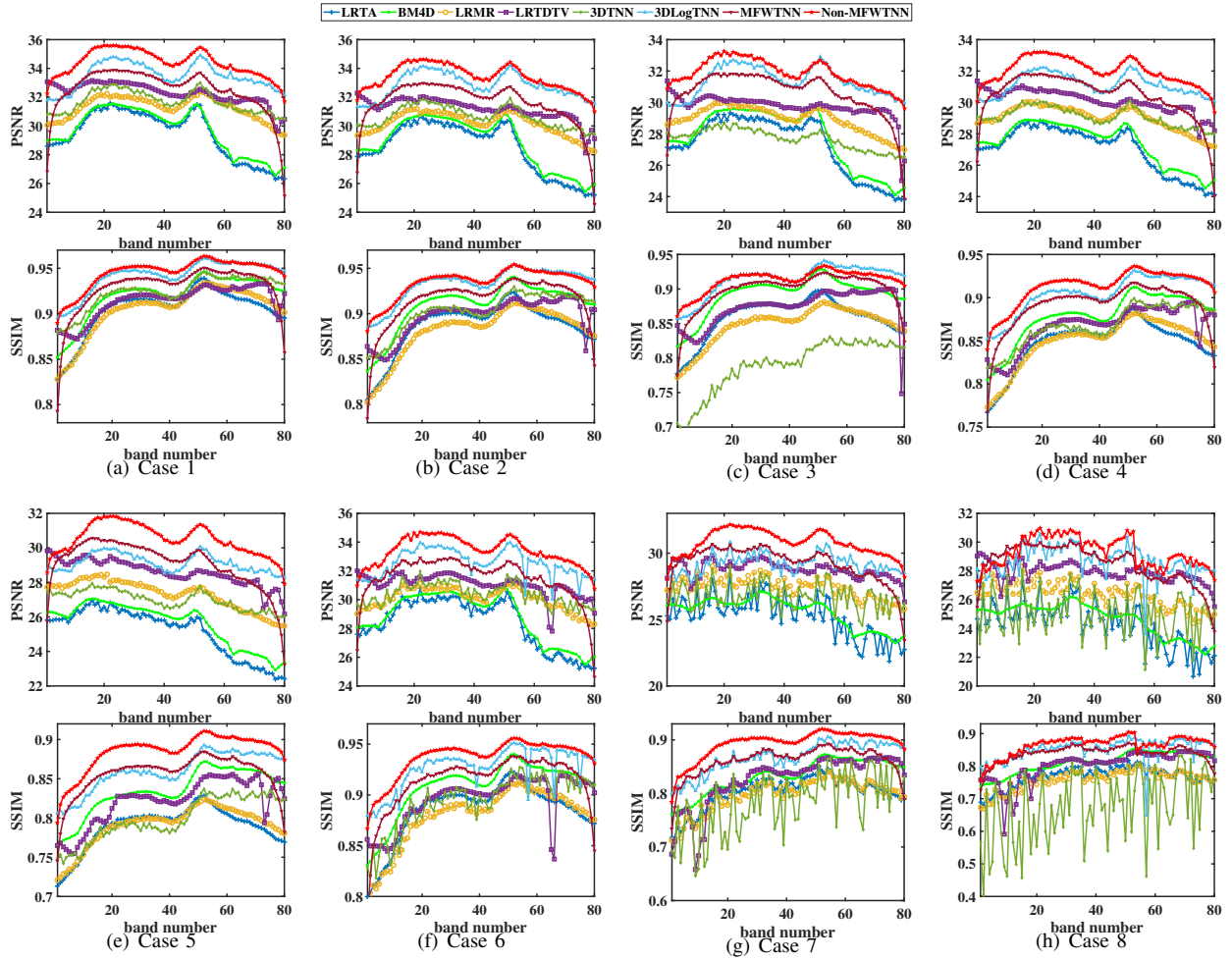


Fig. 7. The PSNR and SSIM of all denoising models for each band under the eight noise cases in Pavia City Center dataset.

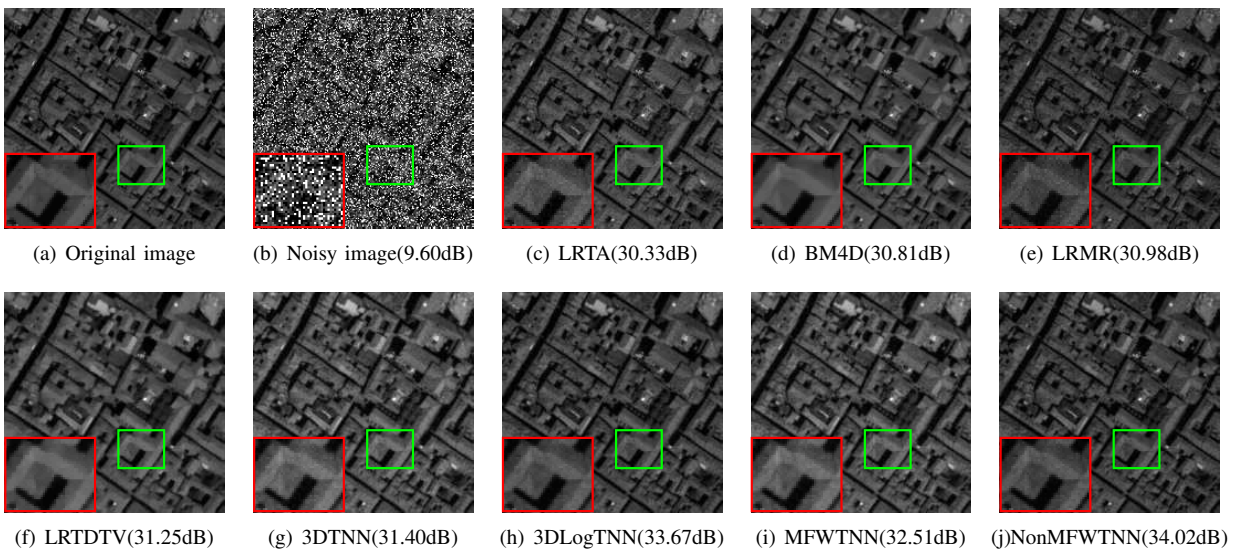


Fig. 8. The 50th band of the denoised results of the Pavia City Center dataset under noise Case 2.

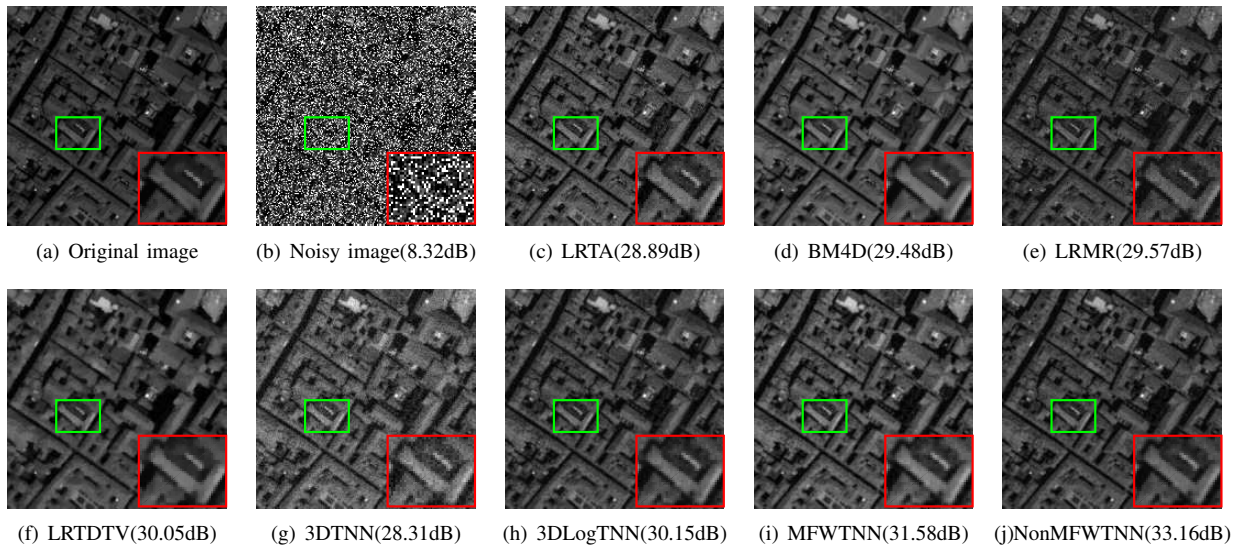


Fig. 9. The 32th band of the denoised results of the Pavia City Center dataset under noise Case 3.

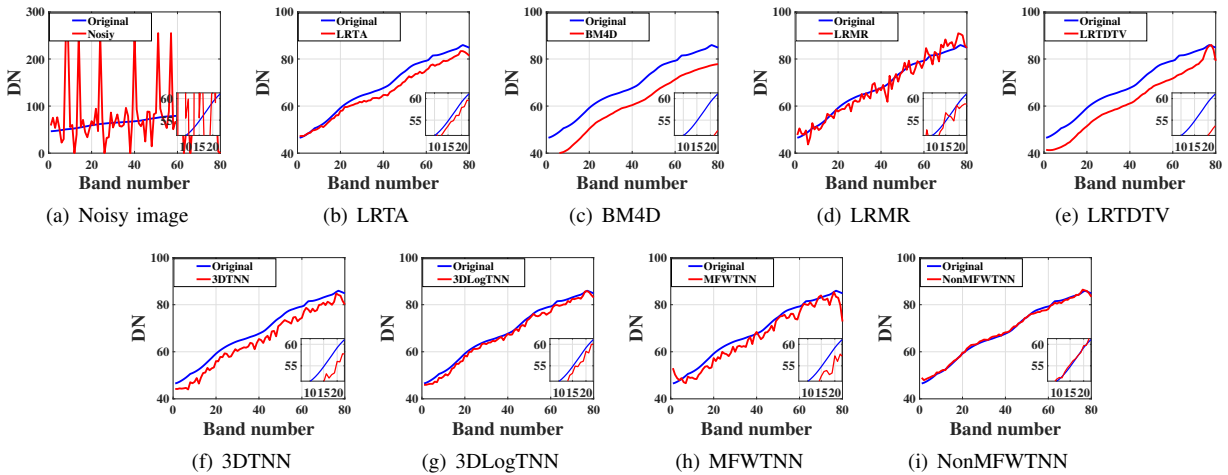


Fig. 10. The Spectral signatures curve of Pavia City Center dataset in (170,99) under noise case 1.

MSSIM values than those of the comparison denoising models. As shown in the Fig. 11, it shows the quantitative comparison with PSNR and SSIM of each band under all noisy cases in the Washington DC Mall dataset, and our methods obtain the optimal PSNR and SSIM values in most bands.

In Fig. 12, we show the 82th band of the denoised results in case 5. In Fig. 13, we show the 57th band of the denoised results in case 7. As these grayscale images show, LRTA, LRMR and 3DTNN cannot completely remove some high-intensity noises and retain more noise. For BM4D and LRTDTV, although they can remove more noise, they also lose more details. This makes the denoised result too smooth. Compared with them, our proposed models can remove more noise while retaining more details. Similar to the Pavia City Center dataset, we show the spectral curve of the pixel (234, 71) under case 6 in Fig. 14. It can be seen that spectral signatures curves are relative to ERGAS values in Table III, and our models can obtain the optimal result.

B. Real HSI Data Experiments

In this subsection, we chose the real HSI dataset in this experiment. It is AVIRIS Indian Pines dataset³. It is filmed by the Airborne Visible Infrared Imaging Spectrometer (AVIRIS). The reason we chose a sub-block with a size of $145 \times 145 \times 220$ as a real dataset is because some bands are seriously polluted by Gaussian white noise and impulse noise and have lost the meaning of reference. We evaluate our denoising model from visual evaluation and vertical average profile. In Fig. 15, we show the 105th band of the observed and denoised results in Indian dataset. It can be seen that it is seriously polluted by Gaussian and sparse noise, and the original ground features information cannot be distinguished. Although the competitive denoising methods restore the feature information of HSI, the denoised HSIs still lose detailed information or residual noise, resulting in missing or blurred texture details of HSI. Our models not only restore more feature information

³<https://engineering.purdue.edu/>

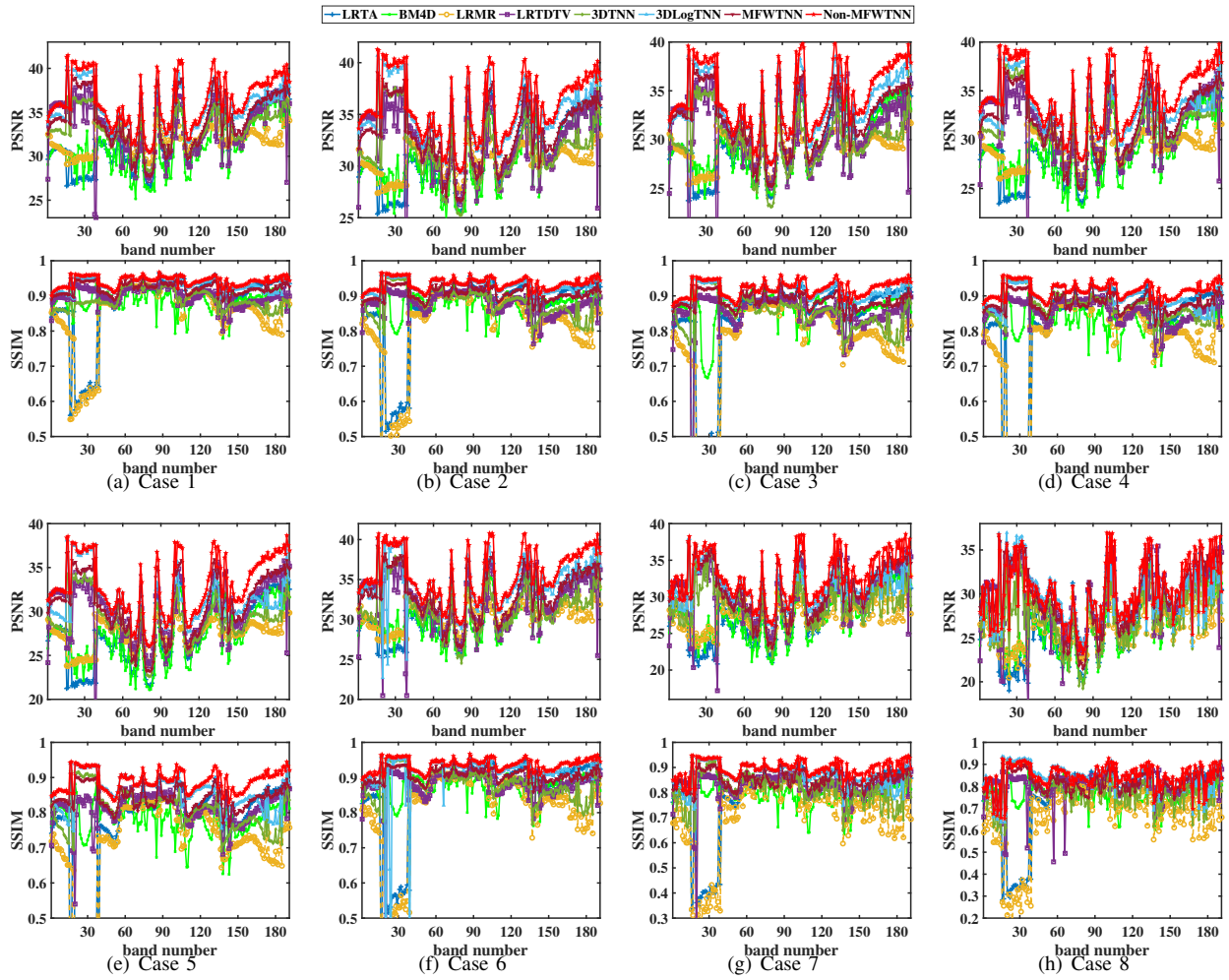


Fig. 11. The PSNR and SSIM of all denoising models for each band under the eight noise cases in Washington DC Mall dataset.

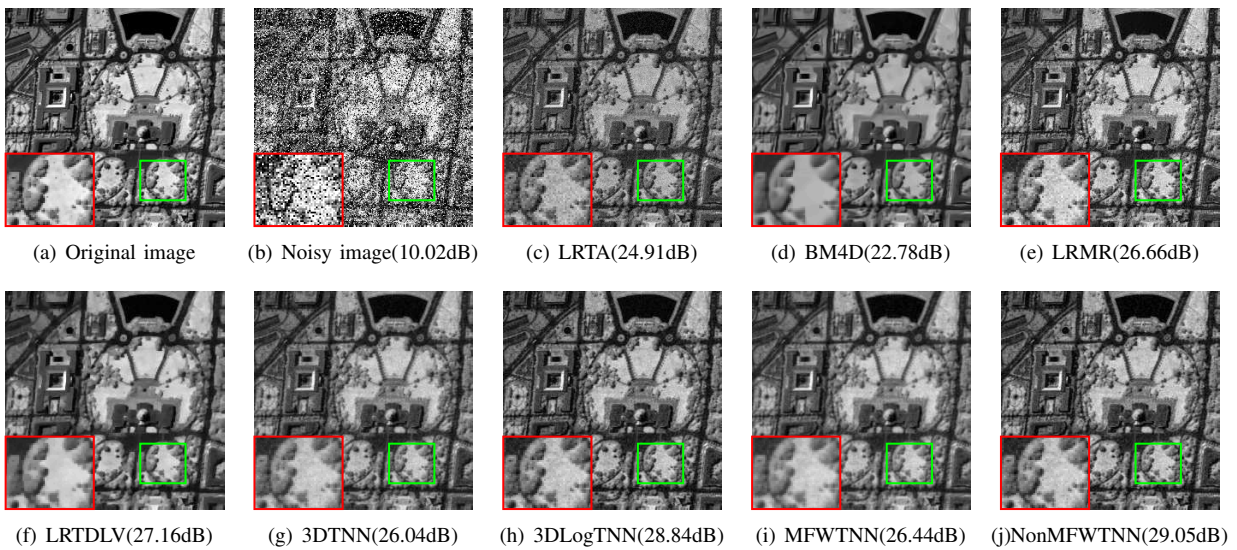


Fig. 12. The 82th band of the denoised results of the Washington DC Mall dataset under noise Case 5.

TABLE III
QUANTITATIVE COMPARISON AND TIME OF EIGHT DENOISING MODELS ON WASHINGTON DC MALL DATASET UNDER EIGHT NOISE CASES.

Case	Level	Index	Noise	LRTA	BM4D	LRMR	LRTDTV	3DTNN	3DLogTNN	MFWTNN	Non-MFWTNN
Case 1	G=0.1	MPSNR	11.024	32.089	31.209	31.856	33.243	33.227	35.518	34.296	36.344
		MSSIM	0.077	0.883	0.889	0.848	0.900	0.889	0.932	0.923	0.942
		MFSIM	0.438	0.938	0.919	0.929	0.931	0.943	0.961	0.950	0.966
	P=0.2	MERGAS	1333.908	104.005	115.882	113.823	96.698	97.016	75.616	86.176	67.825
		MSAM	43.237	4.116	4.519	4.937	4.175	4.136	3.148	3.579	2.864
		time/s	-	56.158	544.679	424.176	545.315	291.548	404.145	330.736	543.209
Case 2	G=0.1	MPSNR	9.420	31.156	30.585	30.595	32.208	31.611	35.030	33.329	35.746
		MSSIM	0.049	0.863	0.878	0.814	0.881	0.882	0.927	0.908	0.935
		MFSIM	0.384	0.928	0.912	0.913	0.919	0.925	0.957	0.941	0.962
	P=0.3	MERGAS	1611.157	115.466	124.189	130.309	110.034	123.077	80.302	96.378	73.121
		MSAM	47.557	4.526	4.805	5.667	4.718	4.885	3.305	3.987	3.052
		time/s	-	55.783	544.675	382.850	539.389	272.741	407.267	330.584	554.722
Case 3	G=0.1	MPSNR	8.253	29.852	29.630	29.149	30.686	29.982	33.579	32.342	34.402
		MSSIM	0.034	0.833	0.859	0.768	0.850	0.851	0.910	0.887	0.922
		MFSIM	0.346	0.911	0.899	0.890	0.901	0.910	0.940	0.928	0.947
	P=0.4	MERGAS	1846.435	133.476	138.002	151.548	133.569	146.816	94.251	108.312	85.311
		MSAM	50.441	5.126	5.262	6.635	6.007	5.955	3.761	4.478	3.490
		time/s	-	57.749	528.381	447.568	584.706	323.020	424.376	370.543	601.149
Case 4	G=0.15	MPSNR	10.635	29.490	28.928	29.286	31.359	31.477	33.121	32.220	34.568
		MSSIM	0.066	0.822	0.834	0.774	0.856	0.874	0.896	0.881	0.916
		MFSIM	0.411	0.906	0.879	0.893	0.902	0.920	0.941	0.923	0.952
	P=0.2	MERGAS	1379.815	138.205	148.879	150.799	120.696	123.227	102.607	109.969	83.629
		MSAM	44.251	5.410	5.774	6.561	5.241	4.979	4.167	4.636	3.518
		time/s	-	59.081	529.783	446.593	585.548	315.768	445.453	366.438	600.614
Case 5	G=0.2	MPSNR	10.188	27.573	27.245	27.427	29.970	28.918	31.223	30.919	33.034
		MSSIM	0.056	0.766	0.783	0.705	0.814	0.809	0.859	0.844	0.891
		MFSIM	0.390	0.877	0.841	0.861	0.875	0.887	0.922	0.900	0.933
	P=0.2	MERGAS	1437.539	170.752	179.235	183.763	141.567	166.078	132.159	127.459	100.032
		MSAM	45.387	6.557	6.845	8.049	6.214	6.782	5.291	5.466	4.167
		time/s	-	54.268	547.776	427.316	540.747	290.324	399.630	340.013	546.367
Case 6	G=0.1	MPSNR	9.512	31.135	30.555	30.572	32.063	31.553	34.525	33.337	35.728
		MSSIM	0.052	0.863	0.878	0.812	0.881	0.882	0.909	0.908	0.937
		MFSIM	0.388	0.927	0.911	0.912	0.920	0.925	0.950	0.941	0.960
	P=(0.2,0.4)	MERGAS	1605.940	116.259	124.905	131.211	112.085	123.948	84.541	96.388	73.122
		MSAM	47.511	4.539	4.814	5.708	4.944	4.934	3.907	3.991	3.045
		time/s	-	54.281	543.748	427.928	541.382	272.044	411.018	331.695	543.483
Case 7	G=(0.1,0.3)	MPSNR	10.175	27.979	27.445	27.667	30.182	29.006	31.356	31.197	32.843
		MSSIM	0.057	0.787	0.795	0.714	0.827	0.815	0.869	0.853	0.895
		MFSIM	0.393	0.886	0.848	0.865	0.883	0.892	0.924	0.906	0.937
	P=0.2	MERGAS	1444.165	165.560	176.071	182.967	142.743	167.263	128.476	124.285	104.171
		MSAM	45.531	6.443	6.700	8.063	6.347	6.934	5.226	5.369	4.389
		time/s	-	53.851	543.508	429.160	534.911	289.693	394.217	336.045	540.726
Case 8	G=(0.1,0.3)	MPSNR	8.937	26.924	26.614	26.396	29.159	27.306	29.804	30.031	30.303
		MSSIM	0.040	0.756	0.771	0.662	0.802	0.778	0.836	0.818	0.844
		MFSIM	0.357	0.868	0.830	0.841	0.870	0.863	0.914	0.887	0.909
	P=(0.2,0.4)	MERGAS	1684.836	186.771	193.299	209.482	165.661	200.091	162.363	144.022	145.351
		MSAM	48.823	7.237	7.322	9.412	7.297	8.633	6.768	6.360	6.325
		stipes	-	60.181	543.885	424.387	532.568	285.417	407.518	341.152	548.572

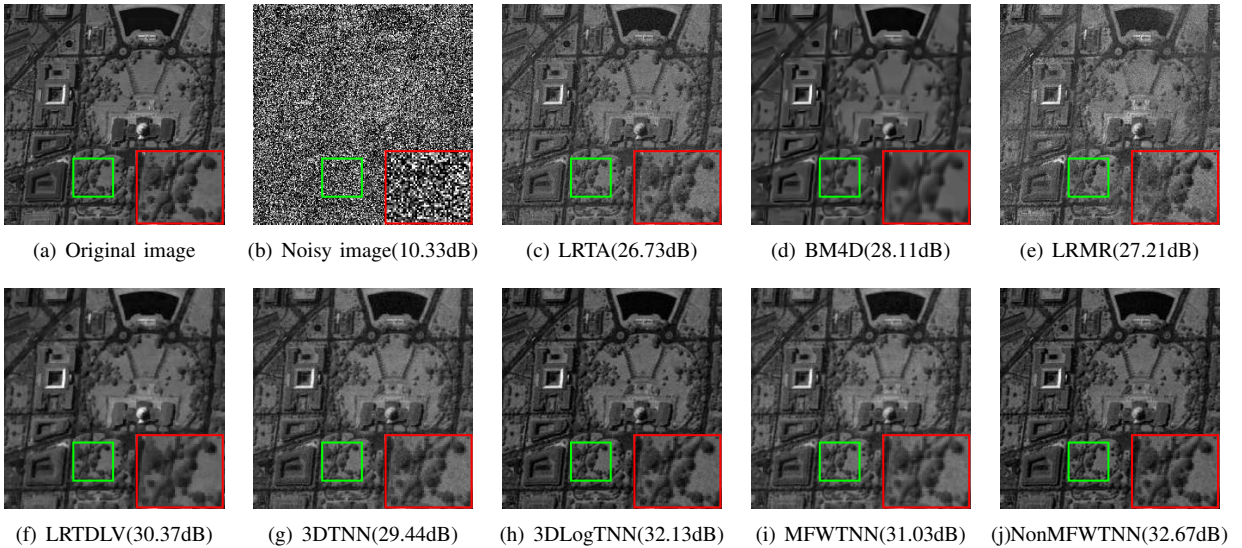


Fig. 13. The 57th band of the denoised results of the Washington DC Mall dataset under noise Case 7.

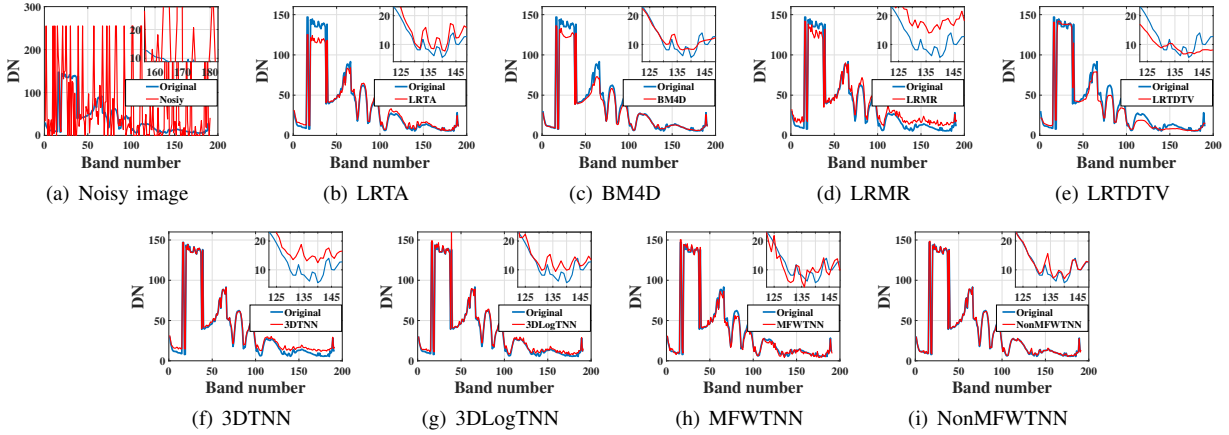


Fig. 14. The Spectral signatures curve of Washington DC Mall in (234,171) under noise case 6

of HSI but also remove more local noise than the competitive methods. Therefore, these denoised HSIs have clearer texture information. In Fig. 16, we show the vertical mean profiles of the 50th band of Indian dataset. Due to the influence of hybrid noises, the vertical mean profiles of the observed HSI shows rapid fluctuations. This means that the smaller fluctuations in the vertical mean profiles, the higher quality of the denoised HSI. Obviously, the mean profile curves obtained by our model are the most stable and its fluctuation is the smallest. This result is relative to the facts reflected in Fig. 15.

C. Discussion

1) Parameter Analysis: In the NonMFWTNN model, five parameters need to be discussed, i.e., the modal weight parameter α , the regularization parameters λ , τ and frequency weight parameter C_1 , and C_2 . All experiments are done under Case 2.

The modal weight α is to control the ratio between different modes. The low-rank characteristics of the spatial dimensions are similar. To reduce the parameters, we set the weights of the two spatial dimensions to equal weights. Therefore, it is set to $\alpha = [1, 1, \alpha_3]/(1 + 1 + \alpha_3)$, which makes $\sum_{i=1}^3 \alpha_i = 1$. We study the impact of α_3 which is selected from $\{0.1 - 1.0\}$ on the robustness of the model, and its optimal value is obtained at 0.2. It can be observed from Fig. 17(a) that when α_3 takes a smaller value, the PSNR value of the denoised result is better. This is because the low-rank characteristic of the spectral mode is stronger than the spatial mode. The regularization parameter τ controls the weight of the Gaussian noise term. Its value is related to the intensity of Gaussian noise. Therefore, it is set to $\tau = \tau_n/\sigma$, where σ is Gaussian noise intensity. We study the impact of τ_n which is selected from $\{10^{-5} - 1.6 \times 10^{-4}\}$ on the robustness of the model, and its optimal value is obtained at 10^{-4} . It can be observed from Fig. 17(c) that when $\tau \leq 0.0001$, the MPSNR of the denoised result is low and fluctuates greatly. The main reason is that when τ is small, the ability to remove Gaussian noise is weak, and there is a lot of remaining Gaussian noise. The regularization parameter λ controls the weight of the sparse noise term. Defining

$$\lambda = \lambda_s \left(\frac{\alpha_1}{\sqrt{\max(n_2, n_3)n_1}} + \frac{\alpha_2}{\sqrt{\max(n_3, n_1)n_2}} + \frac{\alpha_3}{\sqrt{\max(n_1, n_2)n_3}} \right).$$

As observed from Fig. 17(b), our model can obtain remarkable results when λ_s which is selected from $\{0.006 - 0.016\}$. its optimal value is obtained at 0.011. Similar to τ , when λ is small, the noise removal effect is not good. The frequency weight parameter C_1 reflects the scaling ratio of the weight. Fig. 17(d) show the PSNR values when C_1 which is selected from $\{0.1 - 1.0\}$. It can be seen from these figures that when C_1 is small, the frequency weight becomes smaller, and the noise is more difficult to remove; when C_1 is large, the frequency weight becomes larger, and the detailed information of tensor is removed. its optimal value is obtained at 0.6. The frequency weight parameter C_2 reflects the initial weight of the iteration. Fig. 17(e) show the PSNR values when C_2 which is selected from $\{0.1 - 1.0\}$. its optimal value is obtained at 0.6. It shrinks equally of all frequency components. It inherits the advantages of TNN and ensures that noise can be removed correctly.

2) Convergence Analysis: Fig.18 shows the MPSNR value, the MSSIM value, and the Error value of the proposed model according to the iterations. As shown in Fig.18, the number of iterations increases, the value gradually stabilizes by the proposed method, which justifies the numerical convergence of the proposed method.

3) Shortcoming Analysis: The MFWTNN and NonMFWTNN can better explore the low-rank structure of HSI, and achieve excellent results in removing the mixed noise of Gaussian and salt and pepper. But our models do not work for removing dead line noise. On the one hand, our model does not describe prior information for dead line noise. On the other hand, the dead line noise is also low rank, and it is easy to be regarded as a part of HSI, which causes dead line noise to remain in the restored HSI. The following two strategies may solve this shortcoming. Similar to noise modeling of strip noise [64–66], dead line noise can be modeled more accurately. Another solution is to use the PnP framework to integrate the BM3D or deep learning frameworks into the model to achieve the purpose of removing dead line noise [28, 32, 67].

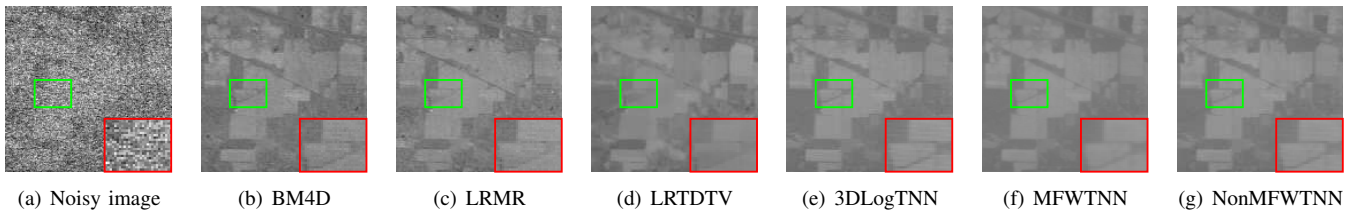


Fig. 15. The 105th band of all denoising results for the Indian dataset.

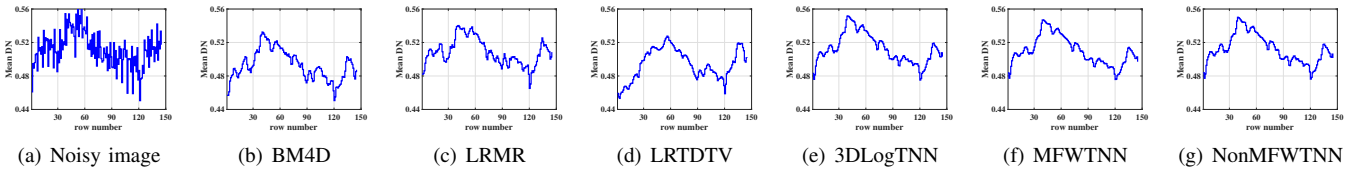


Fig. 16. The vertical mean profiles of band 50 in Indian dataset.

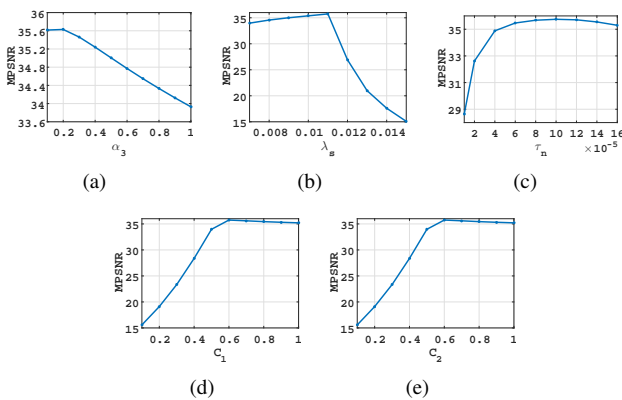


Fig. 17. MPSNR values with respect to different values of parameters.

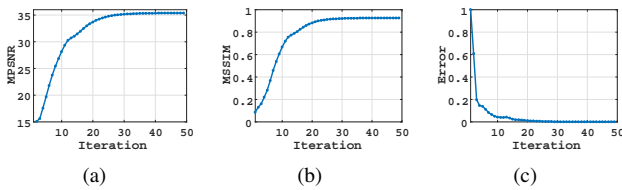


Fig. 18. MPSNR, SSIM and Error values with respect to the number of iterations.

VI. CONCLUSION

In this paper, we proposed the multi-modal and frequency-weighted tensor nuclear norm (MFWTNN) and Non-convex MFWTNN to approximate the rank function and applied them to the HSI denoising task. The MFWTNN not only considered the correlation between two spatial modes and one spectral mode but also considered the frequency meaning of HSI in the Fourier domain. The MFWTNN is the fusion of TNN and SNN, which inherits the advantages of t-SVD and Tucker decomposition. And we gave the frequency weight adaptive calculation way. Since the calculation of weights depends on iteratively restored and observed HSI, our models are more robust to different degrees of noise. It can better characterize the low-rankness of HSI. Besides, based on the MFWTNN

model, we also considered the physical meaning of the internal singular values of the frequency slice and proposed its non-convex approximation. They powerfully improved capability and flexibility for describing low-rankness in HSIs. The experiments conducted with both simulated and real HSI datasets showed that our proposed models based HSI denoising model were competitive methods to remove the hybrid noises.

REFERENCES

- [1] C. Zhao, C. Li, S. Feng, N. Su, and W. Li, “A spectral–spatial anomaly target detection method based on fractional fourier transform and saliency weighted collaborative representation for hyperspectral images,” *IEEE Journal of Selected Topics in Applied Earth Observations and Remote Sensing*, vol. 13, pp. 5982–5997, 2020.
- [2] J. Peng, Y. Zhou, W. Sun, Q. Du, and L. Xia, “Self-paced nonnegative matrix factorization for hyperspectral unmixing,” *IEEE Transactions on Geoscience and Remote Sensing*, 2020.
- [3] D. Hong, L. Gao, N. Yokoya, J. Yao, J. Chanussot, Q. Du, and B. Zhang, “More diverse means better: Multimodal deep learning meets remote-sensing imagery classification,” *IEEE Transactions on Geoscience and Remote Sensing*, 2020.
- [4] H. Zeng, X. Xie, H. Cui, H. Yin, and J. Ning, “Hyperspectral image restoration via global l_{1-2} spatial-spectral total variation regularized local low-rank tensor recovery,” *IEEE Transactions on Geoscience and Remote Sensing*, 2020.
- [5] W. He, H. Zhang, H. Shen, and L. Zhang, “Hyperspectral image denoising using local low-rank matrix recovery and global spatial–spectral total variation,” *IEEE Journal of Selected Topics in Applied Earth Observations and Remote Sensing*, vol. 11, no. 3, pp. 713–729, 2018.
- [6] N. Renard, S. Bourennane, and J. Blanc-Talon, “Denoising and dimensionality reduction using multilinear tools for hyperspectral images,” *IEEE Geoscience and Remote Sensing Letters*, vol. 5, no. 2, pp. 138–142, 2008.

- [7] H. Zhang, W. He, L. Zhang, H. Shen, and Q. Yuan, "Hyperspectral image restoration using low-rank matrix recovery," *IEEE Transactions on Geoscience and Remote Sensing*, vol. 52, no. 8, pp. 4729–4743, 2013.
- [8] W. He, H. Zhang, L. Zhang, and H. Shen, "Total-variation-regularized low-rank matrix factorization for hyperspectral image restoration," *IEEE Transactions on Geoscience and Remote Sensing*, vol. 54, no. 1, pp. 178–188, 2015.
- [9] Q. Xie, Q. Zhao, D. Meng, Z. Xu, S. Gu, W. Zuo, and L. Zhang, "Multispectral images denoising by intrinsic tensor sparsity regularization," in *Proceedings of the IEEE Conference on Computer Vision and Pattern Recognition*, 2016, pp. 1692–1700.
- [10] Y. Chen, Y. Guo, Y. Wang, D. Wang, C. Peng, and G. He, "Denoising of hyperspectral images using nonconvex low rank matrix approximation," *IEEE Transactions on Geoscience and Remote Sensing*, vol. 55, no. 9, pp. 5366–5380, 2017.
- [11] Y. Lou and M. Yan, "Fast l1–l2 minimization via a proximal operator," *Journal of Scientific Computing*, vol. 74, no. 2, pp. 767–785, 2018.
- [12] C. Gao, N. Wang, Q. Yu, and Z. Zhang, "A feasible nonconvex relaxation approach to feature selection," in *Proceedings of the AAAI Conference on Artificial Intelligence*, vol. 25, no. 1, 2011.
- [13] Y. Chen, J. Li, and Y. Zhou, "Hyperspectral image denoising by total variation-regularized bilinear factorization," *Signal Processing*, vol. 174, p. 107645, 2020.
- [14] L. Yang, L. Xu, J. Peng, Y. Song, A. Wong, and D. A. Clausi, "Nonlocal band-weighted iterative spectral mixture model for hyperspectral imagery denoising," *IEEE Transactions on Geoscience and Remote Sensing*, vol. 58, no. 8, pp. 5588–5601, 2020.
- [15] R. A. Harshman and M. E. Lundy, "Parafac: Parallel factor analysis," *Computational Statistics & Data Analysis*, vol. 18, no. 1, pp. 39–72, 1994.
- [16] X. Liu, S. Bourennane, and C. Fossati, "Denoising of hyperspectral images using the parafac model and statistical performance analysis," *IEEE Transactions on Geoscience and Remote Sensing*, vol. 50, no. 10, pp. 3717–3724, 2012.
- [17] L. R. Tucker, "Some mathematical notes on three-mode factor analysis," *Psychometrika*, vol. 31, no. 3, pp. 279–311, 1966.
- [18] J. Liu, P. Musialski, P. Wonka, and J. Ye, "Tensor completion for estimating missing values in visual data," *IEEE Transactions on Pattern Analysis and Machine Intelligence*, vol. 35, no. 1, pp. 208–220, 2012.
- [19] M. E. Kilmer, K. Braman, N. Hao, and R. C. Hoover, "Third-order tensors as operators on matrices: A theoretical and computational framework with applications in imaging," *SIAM Journal on Matrix Analysis and Applications*, vol. 34, no. 1, pp. 148–172, 2013.
- [20] Z. Zhang and S. Aeron, "Exact tensor completion using t-svd," *IEEE Transactions on Signal Processing*, vol. 65, no. 6, pp. 1511–1526, 2016.
- [21] C. Lu, J. Feng, Y. Chen, W. Liu, Z. Lin, and S. Yan, "Tensor robust principal component analysis with a new tensor nuclear norm," *IEEE Transactions on Pattern Analysis and Machine Intelligence*, vol. 42, no. 4, pp. 925–938, 2019.
- [22] C. Mu, B. Huang, J. Wright, and D. Goldfarb, "Square deal: Lower bounds and improved relaxations for tensor recovery," in *International Conference on Machine Learning*. PMLR, 2014, pp. 73–81.
- [23] Q. Yuan, Q. Zhang, J. Li, H. Shen, and L. Zhang, "Hyperspectral image denoising employing a spatial-spectral deep residual convolutional neural network," *IEEE Transactions on Geoscience and Remote Sensing*, vol. 57, no. 2, pp. 1205–1218, 2018.
- [24] A. Maffei, J. M. Haut, M. E. Paoletti, J. Plaza, L. Bruzzone, and A. Plaza, "A single model cnn for hyperspectral image denoising," *IEEE Transactions on Geoscience and Remote Sensing*, vol. 58, no. 4, pp. 2516–2529, 2019.
- [25] Y. Chang, L. Yan, H. Fang, S. Zhong, and W. Liao, "Hsi-denet: Hyperspectral image restoration via convolutional neural network," *IEEE Transactions on Geoscience and Remote Sensing*, vol. 57, no. 2, pp. 667–682, 2018.
- [26] K. Wei, Y. Fu, and H. Huang, "3-d quasi-recurrent neural network for hyperspectral image denoising," *IEEE transactions on neural networks and learning systems*, vol. 32, no. 1, pp. 363–375, 2020.
- [27] Y.-C. Miao, X.-L. Zhao, X. Fu, J.-L. Wang, and Y.-B. Zheng, "Hyperspectral denoising using unsupervised disentangled spatio-spectral deep priors," *IEEE Transactions on Geoscience and Remote Sensing*, vol. 60, pp. 1–16, 2021.
- [28] H. Zeng, X. Xie, H. Cui, Y. Zhao, and J. Ning, "Hyperspectral image restoration via cnn denoiser prior regularized low-rank tensor recovery," *Computer Vision and Image Understanding*, vol. 197–198, p. 103004, 2020.
- [29] Q. Zhang, Q. Yuan, J. Li, F. Sun, and L. Zhang, "Deep spatio-spectral bayesian posterior for hyperspectral image non-iid noise removal," *ISPRS Journal of Photogrammetry and Remote Sensing*, vol. 164, pp. 125–137, 2020.
- [30] Y.-S. Luo, X.-L. Zhao, T.-X. Jiang, Y.-B. Zheng, and Y. Chang, "Hyperspectral mixed noise removal via spatial-spectral constrained unsupervised deep image prior," *IEEE Journal of Selected Topics in Applied Earth Observations and Remote Sensing*, vol. 14, pp. 9435–9449, 2021.
- [31] J.-L. Wang, T.-Z. Huang, X.-L. Zhao, T.-Y. Ji, and T.-X. Jiang, "Hyperspectral denoising via global tensor ring decomposition and local unsupervised deep image prior," in *2021 IEEE International Geoscience and Remote Sensing Symposium IGARSS*. IEEE, 2021, pp. 4119–4122.
- [32] L. Zhuang, M. K. Ng, and X. Fu, "Hyperspectral image mixed noise removal using subspace representation and deep cnn image prior," *Remote Sensing*, vol. 13, no. 20, p. 4098, 2021.
- [33] X. Rui, X. Cao, Q. Xie, Z. Yue, Q. Zhao, and D. Meng, "Learning an explicit weighting scheme for adapting complex hsi noise," in *Proceedings of the IEEE/CVF Conference on Computer Vision and Pattern Recognition*,

- 2021, pp. 6739–6748.
- [34] H. Zeng, Y. Chen, X. Xie, and J. Ning, “Enhanced non-convex low-rank approximation of tensor multi-modes for tensor completion,” *IEEE Transactions on Computational Imaging*, vol. 7, pp. 164–177, 2021.
- [35] H. Fan, Y. Chen, Y. Guo, H. Zhang, and G. Kuang, “Hyperspectral image restoration using low-rank tensor recovery,” *IEEE Journal of Selected Topics in Applied Earth Observations and Remote Sensing*, vol. 10, no. 10, pp. 4589–4604, 2017.
- [36] Y.-B. Zheng, T.-Z. Huang, X.-L. Zhao, T.-X. Jiang, T.-Y. Ji, and T.-H. Ma, “Tensor n-tubal rank and its convex relaxation for low-rank tensor recovery,” *Information Sciences*, vol. 532, pp. 170–189, 2020.
- [37] S. Wang, Y. Liu, L. Feng, and C. Zhu, “Frequency-weighted robust tensor principal component analysis,” *arXiv preprint arXiv:2004.10068*, 2020.
- [38] H. Fan, C. Li, Y. Guo, G. Kuang, and J. Ma, “Spatial-spectral total variation regularized low-rank tensor decomposition for hyperspectral image denoising,” *IEEE Transactions on Geoscience and Remote Sensing*, vol. 56, no. 10, pp. 6196–6213, 2018.
- [39] M. Wang, Q. Wang, J. Chanussot, and D. Li, “Hyperspectral image mixed noise removal based on multidirectional low-rank modeling and spatial-spectral total variation,” *IEEE Transactions on Geoscience and Remote Sensing*, vol. 59, no. 1, pp. 488–507, 2020.
- [40] T. G. Kolda and B. W. Bader, “Tensor decompositions and applications,” *SIAM review*, vol. 51, no. 3, pp. 455–500, 2009.
- [41] Y.-B. Zheng, T.-Z. Huang, X.-L. Zhao, T.-X. Jiang, T.-H. Ma, and T.-Y. Ji, “Mixed noise removal in hyperspectral image via low-fibered-rank regularization,” *IEEE Transactions on Geoscience and Remote Sensing*, vol. 58, no. 1, pp. 734–749, 2019.
- [42] C. J. Hillar and L.-H. Lim, “Most tensor problems are np-hard,” *Journal of the ACM (JACM)*, vol. 60, no. 6, pp. 1–39, 2013.
- [43] M. Fazel, “Matrix rank minimization with applications,” Ph.D. dissertation, PhD thesis, Stanford University, 2002.
- [44] Y. Wang, J. Peng, Q. Zhao, Y. Leung, X.-L. Zhao, and D. Meng, “Hyperspectral image restoration via total variation regularized low-rank tensor decomposition,” *IEEE Journal of Selected Topics in Applied Earth Observations and Remote Sensing*, vol. 11, no. 4, pp. 1227–1243, 2017.
- [45] T.-X. Jiang, M. K. Ng, X.-L. Zhao, and T.-Z. Huang, “Framelet representation of tensor nuclear norm for third-order tensor completion,” *IEEE Transactions on Image Processing*, vol. 29, pp. 7233–7244, 2020.
- [46] B. Madathil and S. N. George, “Dct based weighted adaptive multi-linear data completion and denoising,” *Neurocomputing*, vol. 318, pp. 120–136, 2018.
- [47] W.-H. Xu, X.-L. Zhao, and M. Ng, “A fast algorithm for cosine transform based tensor singular value decomposition,” *arXiv preprint arXiv:1902.03070*, 2019.
- [48] M. K. Ng, X. Zhang, and X.-L. Zhao, “Patched-tube unitary transform for robust tensor completion,” *Pattern Recognition*, vol. 100, p. 107181, 2020.
- [49] E. Kernfeld, M. Kilmer, and S. Aeron, “Tensor-tensor products with invertible linear transforms,” *Linear Algebra and its Applications*, vol. 485, pp. 545–570, 2015.
- [50] T.-X. Jiang, X.-L. Zhao, H. Zhang, and M. K. Ng, “Dictionary learning with low-rank coding coefficients for tensor completion,” *IEEE Transactions on Neural Networks and Learning Systems*, 2021.
- [51] Y.-S. Luo, X.-L. Zhao, T.-X. Jiang, Y. Chang, M. K. Ng, and C. Li, “Self-supervised nonlinear transform-based tensor nuclear norm for multi-dimensional image recovery,” *IEEE Transactions on Image Processing*, 2022.
- [52] H. Kong and Z. Lin, “Tensor q-rank: A new data dependent tensor rank,” *arXiv preprint arXiv:1910.12016*, 2019.
- [53] H. Zeng, X. Xie, and J. Ning, “Hyperspectral image denoising via global spatial-spectral total variation regularized nonconvex local low-rank tensor approximation,” *Signal Processing*, vol. 178, p. 107805, 2021.
- [54] T.-X. Jiang, T.-Z. Huang, X.-L. Zhao, and L.-J. Deng, “Multi-dimensional imaging data recovery via minimizing the partial sum of tubal nuclear norm,” *Journal of Computational and Applied Mathematics*, vol. 372, p. 112680, 2020.
- [55] Y. Liu, L. Chen, and C. Zhu, “Improved robust tensor principal component analysis via low-rank core matrix,” *IEEE Journal of Selected Topics in Signal Processing*, vol. 12, no. 6, pp. 1378–1389, 2018.
- [56] S. Boyd, N. Parikh, and E. Chu, *Distributed optimization and statistical learning via the alternating direction method of multipliers*. Now Publishers Inc, 2011.
- [57] Z. Lin, M. Chen, and Y. Ma, “The augmented lagrange multiplier method for exact recovery of corrupted low-rank matrices,” *arXiv preprint arXiv:1009.5055*, 2010.
- [58] M. Maggioni and A. Foi, “Nonlocal transform-domain denoising of volumetric data with groupwise adaptive variance estimation,” in *Computational Imaging X*, vol. 8296. International Society for Optics and Photonics, 2012, p. 82960O.
- [59] Q. Huynh-Thu and M. Ghanbari, “Scope of validity of psnr in image/video quality assessment,” *Electronics Letters*, vol. 44, no. 13, pp. 800–801, 2008.
- [60] Z. Wang, A. C. Bovik, H. R. Sheikh, E. P. Simoncelli *et al.*, “Image quality assessment: from error visibility to structural similarity,” *IEEE Transactions on Image Processing*, vol. 13, no. 4, pp. 600–612, 2004.
- [61] L. Zhang, L. Zhang, X. Mou, and D. Zhang, “FSIM: A feature similarity index for image quality assessment,” *IEEE Transactions on Image Processing*, vol. 20, no. 8, pp. 2378–2386, 2011.
- [62] L. Wald, *Data fusion: definitions and architectures: fusion of images of different spatial resolutions*. Presses des MINES, 2002.
- [63] F. Kruse, A. Lefkoff, and J. Dietz, “Expert system-based mineral mapping in northern death valley, california/nevada, using the airborne visible/infrared imaging spectrometer (aviris),” *Remote Sensing of Environment*, vol. 44, no. 2-3, pp. 309–336, 1993.
- [64] H. Zhang, J. Cai, W. He, H. Shen, and L. Zhang, “Double

low-rank matrix decomposition for hyperspectral image denoising and destriping,” *IEEE Transactions on Geoscience and Remote Sensing*, vol. 60, pp. 1–19, 2021.

- [65] F. Yang, X. Chen, and L. Chai, “Hyperspectral image destriping and denoising using stripe and spectral low-rank matrix recovery and global spatial-spectral total variation,” *Remote Sensing*, vol. 13, no. 4, p. 827, 2021.
- [66] Y. Chen, T.-Z. Huang, L.-J. Deng, X.-L. Zhao, and M. Wang, “Group sparsity based regularization model for remote sensing image stripe noise removal,” *Neurocomputing*, vol. 267, pp. 95–106, 2017.
- [67] Y.-Y. Liu, X.-L. Zhao, Y.-B. Zheng, T.-H. Ma, and H. Zhang, “Hyperspectral image restoration by tensor fibered rank constrained optimization and plug-and-play regularization,” *IEEE Transactions on Geoscience and Remote Sensing*, vol. 60, pp. 1–17, 2021.

APPENDIX A APPENDIX

Lemma 1. [9] Let $0 < \tau$ and $0 < \varepsilon < \min\left(\sqrt{\tau}, \frac{\tau}{y}\right)$, the following problem:

$$\min_x f(x) = \tau \log(|x| + \varepsilon) + \frac{1}{2}(x - y)^2 \quad (30)$$

has a local minimal

$$\mathcal{D}_{\tau, \varepsilon}(y) = \begin{cases} 0 & \text{if } c_2 \leq 0 \\ \text{sign}(y) \left(\frac{c_1 + \sqrt{c_2}}{2}\right) & \text{if } c_2 > 0 \end{cases} \quad (31)$$

where $c_1 = |y| - \varepsilon$ and $c_2 = (c_1)^2 - 4(\tau - \varepsilon|y|)$.

Theorem 1. For any positive threshold $\tau > 0$, $\mathcal{Y} \in \mathbb{R}^{n_1 \times n_2 \times n_3}$, and frequency weighting w , parameter $\varepsilon > 0$, the following problem:

$$\underset{\mathcal{X}}{\text{argmin}} \tau \|\mathcal{X}\|_{FW^*, \text{Log}} + \frac{1}{2} \|\mathcal{X} - \mathcal{Y}\|_F^2 \quad (32)$$

is given by the double-weighted tensor singular value thresholding

$$\mathcal{X}^* = \mathcal{D}\mathcal{W}^{w, \tau, \varepsilon}(\mathcal{Y}) = \mathcal{U} * \mathcal{S}^{w, \tau, \varepsilon} * \mathcal{V}^H, \quad (33)$$

where $\mathcal{Y} = \mathcal{U} * \mathcal{S} * \mathcal{V}^H$, $\mathcal{S}^{w, \tau, \varepsilon} = \text{ifft}\left(\left(\overline{\mathcal{S}}\right)^{w, \tau, \varepsilon}\right)$ and

$$\left(\overline{\mathcal{S}}\right)^{w, \tau, \varepsilon}(i, j, s) = \begin{cases} 0, & \text{if } c_2 \leq 0 \\ \text{sign}\left(\overline{\mathcal{S}}(i, j, s)\right) \left(\frac{c_1 + \sqrt{c_2}}{2}\right), & \text{if } c_2 > 0 \end{cases} \quad (34)$$

where $\overline{\mathcal{S}} = \text{fft}(\mathcal{S})$, $c_1 = \left|\overline{\mathcal{S}}(i, j, s)\right| - \varepsilon$, and $c_2 = c_1^2 - 4(w_k \tau - \varepsilon \left|\overline{\mathcal{S}}(i, j, s)\right|)$

Proof. According to the properties of the tensor in the Fourier domain, the problem (32) is equivalent to

$$\begin{aligned} & \arg \min \tau \|\mathcal{X}\|_{FW^*, \text{Log}} + \frac{1}{2} \|\mathcal{X} - \mathcal{Y}\|_F^2 \\ \Leftrightarrow & \arg \min \tau \frac{1}{n_3} \sum_{k=1}^{n_3} w_k \log\left(\|\overline{\mathbf{X}}^{(k)}\|_*\right) + \frac{1}{2n_3} \|\overline{\mathcal{X}} - \overline{\mathcal{Y}}\|_F^2 \\ \Leftrightarrow & \arg \min \frac{1}{n_3} \sum_{k=1}^{n_3} \tau w_k \sum_{i=1}^{\min(n_1, n_2)} \log\left(\sigma_i\left(\overline{\mathbf{X}}^{(k)}\right) + \varepsilon\right) \\ & + \frac{1}{2} \|\overline{\mathbf{X}}^{(k)} - \overline{\mathbf{Y}}^{(k)}\|_F^2. \end{aligned} \quad (35)$$

Therefore, the problem in (32) can be divided into n_3 subproblems about problem (30). From Lemma 1, for k subproblems, its solution is

$$\overline{\mathbf{X}}^{(k)} = \mathcal{D}_{w_k \tau, \varepsilon}(\overline{\mathbf{Y}}^{(k)}) = \begin{cases} 0 & \text{if } c_2 \leq 0 \\ \text{sign}(\overline{\mathbf{Y}}^{(k)}) \left(\frac{c_1 + \sqrt{c_2}}{2}\right) & \text{if } c_2 > 0 \end{cases} \quad (36)$$

□